RESEARCH ARTICLE | SEPTEMBER 24 2025

The effect of endplates on vortex-induced vibration of finite-length cylinders

Andrei Fershalov ; Niell Elvin ; Daniel Struk ; Denise Morocho Romero ; Pieter Orlandini ; Yang Liu

Physics of Fluids 37, 094139 (2025)
https://doi.org/10.1063/5.0289566
CHORUS

Physics of Fluids ARTICLE pubs.aip.org/aip/pof

The effect of endplates on vortex-induced vibration of finite-length cylinders

Cite as: Phys. Fluids **37**, 094139 (2025); doi: 10.1063/5.0289566
Submitted: 8 July 2025 · Accepted: 10 September 2025 ·
Published Online: 24 September 2025

Andrei Fershalov, Niell Elvin, Daniel Struk, Denise Morocho Romero, Pieter Orlandini, and Yang Liu[a)]

AFFILIATIONS

Department of Mechanical Engineering, The City College of New York, New York, New York 10031, USA

[a)]Author to whom correspondence should be addressed: yliu7@ccny.cuny.edu

ABSTRACT

This study experimentally investigates the three-dimensional (3-D) effects of a cylinder oscillator energy harvester system in terms of vortex-induced vibration (VIV). The 3-D effects were modulated by varying endplate size. Specifically, these effects were evaluated by examining the influence of different endplate sizes on aerodynamic forces and vibrational amplitudes of the finite-length cylinder oscillator. Two configurations were studied: a rigidly mounted stationary cylinder as a reference, and a flexibly mounted cylinder oscillating transversely in airflow, both with the same diameter. The Reynolds number range was ∼5300–21 300. Adding circular endplates to the stationary cylinder significantly increased lift fluctuations, while an endplate diameter three times the cylinder was sufficient to suppress spanwise end effects. These findings informed the VIV experiments, where bare and endplate (various diameters) configurations were evaluated under matched structural parameters. While the addition of endplates did not alter the lock-in bandwidth, they strongly influenced aerodynamic forces and vibration amplitude within the lock-in regime. Smaller endplates (two times diameter) enhanced peak vibration amplitude, despite added mass, indicating a net gain in energy harvesting. In contrast, larger endplates (three times diameter) generally reduced vibration amplitude and induced earlier transition to the lower VIV branch, despite producing the highest lift coefficients. Phase and frequency analysis revealed configuration-specific differences, especially beyond an amplitude ratio of 0.3. In the post-lock-in regime, organized vortex shedding persisted only for the larger endplate cylinder, but was absent for both the bare and smaller-endplate cylinders.

NOMENCLATURE

AR	cylinder aspect ratio
A^*_{peak}	peak amplitude ratio
A^*	amplitude ratio
C_A	the ideal added mass coefficient
C_D	instantaneous drag coefficient
C_D^{mean}	time-averaged (mean) drag coefficient
C_L	instantaneous lift coefficient
C_L^{RMS}	root mean square of the lift coefficient
$\bar{C}_L$	magnitude of the lift coefficient fluctuation
Cp	pressure coefficient
C_p^{STD}	standard deviation of the pressure coefficient
C_{piezo}	piezo capacitance
c	structural damping (kg/s)
D	diameter of the cylinder (m)
D_{ep}	diameter of the endplates (m)
E	elastic modulus of the beam (Pa)
F_D	drag force (N)
F_L	lift force (N)
$\bar{F}_L$	magnitude of the lift force (N)
f	vibration frequency (Hz)
f_n	natural frequency of the vibrating structure (Hz)
f_v	vortex shedding frequency (Hz)
f^*	frequency ratio
h_b	height of the beam (m)
k	structural stiffness (N/m)
L	length of the cylinder (m)
l_b	length of the beam(m)
m	vibrating mass (kg)
m^*	mass ratio
P	the instantaneous power input (W)
$\bar{P}$	the time-averaged power input in one cycle (W)
$P_{piezo,opt}$	optimal electrical power harvested from the system (W)
$P^*_{piezo,opt}$	optimal dimensionless electrical power harvested from the system
p	local static pressure on the cylinder surface (Pa)
p_∞	free-stream static pressure (Pa)

Re	Reynolds number
St	Strouhal number
T	vibration period (s)
t	time (s)
t_b	thickness of the beam (m)
U_∞	free stream velocity (m/s)
U^*	reduced velocity
ν	kinematic viscosity of the fluid (m^2/s)
Y	amplitude of vibration (m)
y	deflection of the beam tip (m)
α	angle between absolute velocity and free stream velocity (°)
δ_{st}	static deflection (m)
ζ	damping ratio
θ	the angular position of a pressure probe around the cylinder circumference (°)
θ_{piezo}	the electromechanical coupling parameter (N/V)
ρ	fluid density (kg/m^3)
ρ_b	density of the beam (kg/m^3)
φ	phase angle (°)
ω	angular frequency (rad/s)
ω_n	angular natural frequency (rad/s)

I. INTRODUCTION

The flow around circular cylinders is a fundamental problem in fluid dynamics, which occurs in a wide-range of engineering applications, including offshore structures, bridge cables, heat exchanger tubes, and small-scale energy harvesters. While the flow past infinitely long or high-aspect-ratio cylinders has been extensively studied, real-world systems often feature cylinders of finite length, where end effects and three-dimensional flow structures strongly influence wake development and applied fluid forces.

Endplates are frequently employed in both experimental and industrial contexts to mitigate spanwise flow and stabilize vortex shedding. For stationary cylinders, numerous studies have shown that endplate geometry significantly alters the wake structure, drag, and lift forces by suppressing three-dimensional instabilities near the free ends.[1–3]

Potts *et al.*[1] investigated the influence of aspect ratio and end conditions on the drag of stationary, circular cylinders through controlled tow tank experiments and compared them with data in the literature. Experimental results confirmed that drag is significantly affected by the presence of tip vortices, especially for cylinders with the aspect ratio (AR) below 13, and that endplates with diameters greater than three times the cylinder diameter can effectively suppress vortex shedding near the free end.

Farell and Fedeniuk[2] conducted an experimental study on the flow over circular, stationary cylinders with and without endplates at critical and transcritical Reynolds numbers. Their findings showed that endplates significantly modified the flow characteristics, leading to notable changes in base and minimum pressure coefficients—up to 15%–20% in some cases—and altered vortex shedding behavior.

Norberg[3] conducted an extensive experimental study on the influence of aspect ratio and endplate geometry on the flow around a stationary, circular cylinder at Reynolds numbers ranging from 50 to 4×10^4. The study found that large aspect ratios are essential for minimizing end effects, especially in the laminar shedding regime, where parallel shedding is strongly influenced by local velocity gradients near the cylinder ends. The research highlighted that aspect ratios (AR) of 60–70 are needed in the subcritical regime for flow behavior to resemble that of a quasi-infinite cylinder. In Ref. 4, a comprehensive study of the fluctuating lift forces acting on stationary circular cylinders under a wide range of Reynolds numbers was conducted. The findings provide a critical framework for understanding three-dimensional effects and spanwise coherence in bluff body flows, which are particularly relevant when evaluating force fluctuations and structural response in finite-length cylinders.

While numerous studies have investigated VIV behavior of finite-length cylinders in the absence of endplates,[5–12] the addition of endplates under dynamic fluid-structure interaction conditions remains underexplored. The vibratory response of cylinders with spanwise free ends is strongly dependent on the aspect ratio.[13,14] When only one end is free, a distinct response known as end-cell-induced vibration (ECIV) can emerge—particularly at higher fluid velocities—coexisting with traditional VIV modes.[14] At low aspect ratios, although vortex shedding persists, it becomes weaker and more disorganized, suppressing the likelihood of high-amplitude oscillations.[5,14]

The limited knowledge about the effectiveness of endplates in VIV regimes highlights a key knowledge gap, especially given the increasing interest in using VIV as a mechanism for energy harvesting. Vortex-induced vibrations arise when alternate vortex shedding synchronizes with a structure's natural frequency, producing large oscillations over a range of flow velocities—a phenomenon known as "lock-in."[5,7] Traditionally viewed as a source of structural fatigue, VIV has more recently been reenvisioned as a viable strategy for renewable energy production, particularly through piezoelectric transduction in small-scale systems.[15–18] In such configurations, flexible structures like cantilever-mounted cylinders convert mechanical strain from VIV into electrical power via surface-mounted piezoelectric elements.[19] The energy harvesting performance is highly sensitive to oscillation amplitude, frequency, and the phase relationship between aerodynamic forces and the structural response.[20–23]

Recent studies have introduced a variety of innovative strategies aimed at enhancing the efficiency of piezoelectric-based VIV energy harvesters. For instance, slit-offset and non-uniform cylinder designs have been shown to significantly increase vibration amplitude, thereby improving energy conversion at low Reynolds numbers.[24,25] Hybrid systems combining piezoelectric and electromagnetic mechanisms have demonstrated enhanced performance under VIV conditions.[26,27] Comprehensive reviews have further cataloged emerging techniques and configurations aimed at maximizing flow-induced piezoelectric energy harvesting.[28,29] Several experimental investigations have validated practical optimization strategies for circular cylinder harvesters.[30–32] Additionally, aerodynamic tailoring of cylinder geometry has been explored to improve aeroelastic behavior and energy extraction efficiency;[33] furthermore, recent advances in multi-directional and multi-modal VIV systems have opened new possibilities for broadening the operational bandwidth and improving energy harvesting yield under variable wind conditions.[34]

Wake-oscillator models are widely used to represent the near wake by a van-der-Pol–type oscillator that is nonlinearly coupled to the structural degree of freedom; representative formulations and applications are discussed in Refs. 35–37 These semi-empirical models reproduce many qualitative features of lock-in and amplitude scaling,

but their coupling coefficients and nonlinear terms are typically identified from experimental data; furthermore, standard implementations assume a spanwise-coherent wake or require explicit multi-mode augmentation to represent spanwise variation.[36] Consequently, while wake-oscillator frameworks remain powerful for two-dimensional or spanwise-coherent VIV,[36] they do not inherently capture tip-region confinement or the three-dimensional wake restructuring induced by endplates without additional three-dimensional modeling or targeted parameter identification.

Following the discussion above, the 3-D effects of finite-length cylinders and the mitigating approach of using endplates on VIV-based oscillator energy harvesters remain underexplored. This motivates the need for detailed experimental studies exploring induced flows and vibrational features of a finite-length cylinder oscillator due to the 3-D effects, and examining how the use of endplates would suppress the spanwise flow, thus modulating the force generation and vibration behavior in the VIV oscillator energy systems.

In this study, a series of experiments were conducted to investigate the influence of endplate size on the aerodynamic forces and wake behavior of a finite-length cylinder, with particular emphasis on improving energy harvesting from VIV. Two flow regimes were examined: (i) a stationary configuration with the cylinder rigidly mounted, conducted as a reference to guide endplate selection and to characterize baseline flow conditions, and (ii) a flexibly mounted configuration where the cylinder was allowed to oscillate transversely under VIV conditions.

Extensive wind tunnel tests were conducted, integrating pressure measurements, strain gauge-based motion tracking, and flow visualization to capture synchronized data on the force coefficients, the wake patterns, and the structural response. Special focus is placed on evaluating how endplates (of different sizes) affect lift force fluctuations, phase angle dynamics, and the energy input into the system, which are critical factors for the design and optimization of VIV-based energy harvesters.

II. THEORETICAL BACKGROUND

The flow around a circular cylinder is a classical problem in bluff-body aerodynamics, characterized by flow separation, unsteady vortex shedding, and strong Reynolds number dependence. When a uniform flow impinges on a stationary circular cylinder, a stagnation point forms on the front surface, and the flow accelerates around the sides, creating regions of low pressure near the lateral surfaces.

The pressure coefficient C_p is a dimensionless parameter used to describe the pressure distribution around the cylinder and is defined as $C_p = \frac{p-p_\infty}{\frac{1}{2}\rho U_\infty^2}$, where p is the local static pressure on the surface, p_∞ is the free-stream static pressure, ρ is the fluid density, and U_∞ is the free-stream velocity. A negative C_p indicates suction (low-pressure) regions, which typically occur along the sides of the cylinder due to flow acceleration and boundary layer separation. Flow separation occurs approximately at an angular position of 60°–120° from the front stagnation point, depending on the Reynolds number and surface conditions. This separation leads to the formation of a turbulent wake behind the cylinder, composed of various vortex structures, which is responsible for fluctuating forces.

The drag coefficient C_D and lift coefficient C_L quantify the normalized streamwise and transverse forces, respectively, and are defined as $C_D = \frac{F_D}{\frac{1}{2}\rho U_\infty^2 DL}$ and $C_L = \frac{F_L}{\frac{1}{2}\rho U_\infty^2 DL}$, where F_D and F_L are the drag and lift forces acting on the cylinder, D is the cylinder diameter, and L is the span (or length) of the cylinder exposed to the flow.

An important dimensionless quantity describing the frequency of vortex shedding is the Strouhal number (St), defined as $St = \frac{f_v D}{U_\infty}$, where f_v is the vortex shedding frequency. For a smooth, stationary circular cylinder in the subcritical Reynolds number regime (approximately $10^3 < Re < 2 \times 10^5$), the Strouhal number remains relatively constant at around 0.18–0.2.[23]

The behavior of the flow and its associated force coefficients are strongly influenced by the Reynolds number (Re), defined as $Re = \frac{U_\infty D}{\nu}$, where ν is the kinematic viscosity of the fluid. At low Reynolds numbers, the flow remains steady and attached; as Re increases, the boundary layer transitions, separation occurs earlier, and vortex shedding becomes more pronounced.[38] At very high Reynolds numbers, additional wake instabilities and turbulence dominate the flow behavior.[38]

For the case of a flexibly mounted cylinder, vortex-induced vibrations arise when the vortex shedding frequency approaches the natural frequency of the system, resulting in large-amplitude oscillations. This leads to the so-called "lock-in" phenomenon, where the vortex shedding frequency synchronizes with the cylinder's natural frequency over a range of flow velocities.[5–7,23] During VIV, the mass ratio—defined as the ratio of the structural mass of the cylinder to the mass of the displaced fluid—plays a significant role in governing the system's dynamic response. The mass ratio is given by $m^* = \frac{m}{\rho \pi D^2 L/4}$, where m is the vibrating mass.

A lower mass ratio generally results in higher peak vibration amplitudes and a broader lock-in bandwidth, while a higher mass ratio tends to suppress oscillation amplitudes and narrow the lock-in regime.[9,23] Thus, mass ratio is a critical parameter affecting energy transfer, vibration behavior, and fluid-structure interaction dynamics during vortex-induced vibration.

Figure 1 presents an overview of the system and a representative amplitude response for a circular cylinder undergoing vortex-induced vibration (VIV).[23] The schematic in Fig. 1(a) illustrates the energy harvester configuration, where a finite-length cylinder is flexibly mounted on cantilever beams and allowed to oscillate in the cross-flow direction. Figure 1(b) shows the amplitude response of the cylinder, where the vibration amplitude Y is normalized by the cylinder diameter D and expressed as the amplitude ratio $A^* = Y/D$. The response is plotted against the reduced velocity, defined as $U^* = U_\infty/(f_n D)$, where $f_n = \omega_n/2\pi$ is the natural frequency of the system, where ω_n is the angular natural frequency of the system. The characteristic VIV behavior—including the pre-lock-in, lock-in, and post-lock-in regimes—is clearly captured in the curve, with a distinct amplitude peak occurring within the lock-in range.

At low flow velocities, the cylinder remains motionless due to insufficient aerodynamic excitation (pre-lock-in). As the flow speed increases, the frequency of vortex shedding rises and approaches the natural frequency of the structure (f_n). Once this frequency match is achieved, the system enters the lock-in region, where the flow-induced forces synchronize with the structural response, resulting in large-amplitude oscillations. This lock-in regime spans a range of reduced velocities U^*, reflecting a strong interaction between the fluid forces and the cylinder's dynamics. Beyond this range, as the flow velocity continues to increase, the shedding frequency uncouples from the natural frequency, and the vibration amplitude diminishes, signaling the end of the lock-in region (post-lock-in).

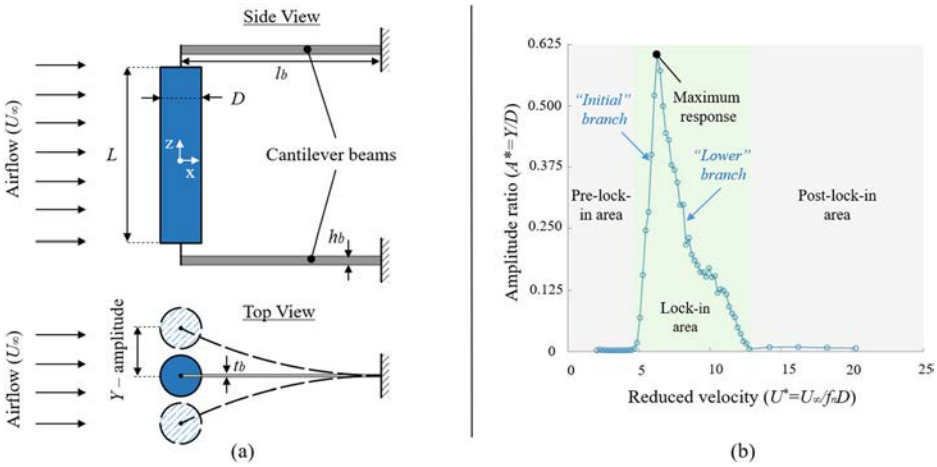

FIG. 1. (a) Schematic of the VIV energy harvester, showing a finite-length circular cylinder mounted on elastic cantilever beams.[23] (b) Representative amplitude response curve of the cylinder from Ref. 23.

The cross-flow motion of the cylinder can be effectively represented by a single-degree-of-freedom (SDOF) model,

$$m\ddot{y} + c\dot{y} + ky = F_L(t), \tag{1}$$

where m is the mass, c is the damping coefficient, k is the stiffness of the system; y is the displacement, where the over-dot (i.e., $\dot{y}$ and $\ddot{y}$) indicate derivatives with respect to time, and $F_L(t)$ is the time-dependent lift force, which can be defined as

$$F_L(t) = C_L(t) \cdot \frac{1}{2}\rho U_\infty^2 DL. \tag{2}$$

For large-amplitude, steady-state, vortex-induced oscillations, the fluid force, and the body displacement response oscillate at the same frequency (f), which is usually close to natural frequency $f_n = \frac{1}{2\pi}\sqrt{\frac{k}{m}}$.

When a bluff body is responding to vortex shedding, the fluid force must lead the excitation by some phase angle φ,

$$y(t) = Y\cos(\omega t - \varphi), \tag{3}$$

$$C_L(t) = \bar{C}_L\cos(\omega t), \tag{4}$$

where $\omega = 2\pi f$ is the angular frequency, Y is the magnitude of vibration, and $\bar{C}_L$ is the magnitude of the lift coefficient fluctuation.

The frequency ratio equation was derived in terms of the system parameters as given in Ref. 5,

$$\frac{f_n}{f} = \left[1 - \frac{\bar{C}_L}{4\pi^2}\cos\varphi\left(\frac{\rho D^2}{2m}\right)\left(\frac{U_\infty}{f_n D}\right)\left(\frac{Y}{D}\right)^{-1}\right]^{-1/2}. \tag{5}$$

This demonstrates that the vibration frequency is close to the natural frequency of the system, particularly in air, where $\left(\frac{\rho D^2}{2m}\right) \sim 10^{-3}$.

Assuming a purely harmonic excitation force and a steady-state response of the system, the magnitude of vibration Y and the phase angle φ can be represented in a set of dimensionless parameters,[39]

$$Y = \frac{\delta_{st}}{\sqrt{\left(1-(f^*)^2\right)^2 + (2\zeta f^*)^2}}, \tag{6}$$

$$\varphi = \tan^{-1}\left(\frac{2\zeta f^*}{1-(f^*)^2}\right), \tag{7}$$

where $\delta_{st} = \bar{F}_L/k$ is the static deflection, $\bar{F}_L = \bar{C}_L\frac{1}{2}\rho U_\infty^2 DL$ is the magnitude of the lift force, $f^* = f/f_n$ is the frequency ratio, and $\zeta = \frac{c}{2\sqrt{km}}$ is the damping ratio.

The instantaneous power $P(t)$ delivered from the fluid to the structure is

$$P(t) = F_L(t)\cdot\dot{y}(t). \tag{8}$$

The time-averaged power input from the fluid into the system over one cycle is then

$$\bar{P}(t) = \frac{1}{T}\int_0^T P(t)dt = \frac{1}{2}\bar{F}_L Y\omega\sin(\varphi). \tag{9}$$

It can be seen that the power input is proportional to the amplitude, the force magnitude, the frequency, and most importantly, the sine of the phase angle. Based on Eq. (9), to generate positive energy input into the system, the phase angle between the cylinder motion and the lift force must lie between 0° and 180°, with maximum power transfer occurring near 90°.

Assuming the lift force is independent of cylinder motion, the system behaves like a linear, forced oscillator: in the pre-lock-in regime, it responds quasi-statically with minimal phase lag; near resonance (lock-in), force, and displacement synchronize with a 90° phase lag; and in the post-lock-in regime, the response is inertia-dominated with the displacement nearly 180° out of phase. This simplified view neglects the dynamic coupling between the flow and structural motion.

However, in the context of vortex-induced vibration, the fluid force is intrinsically coupled to the cylinder's motion. The vortex shedding process is dynamically influenced by the structure's displacement and velocity, resulting in a nonlinear, self-excited fluid-structure interaction. As a result, traditional assumptions about pre-lock-in, lock-in, and post-lock-in regimes may not fully capture the complex dynamics of a flexibly mounted system. This coupling alters not only the amplitude of vibration but also the instantaneous phase and magnitude of the aerodynamic forces, all of which are critical to the system's performance as an energy harvester.

For energy harvesting applications, the goal is to maximize the net mechanical power input from the fluid to the structure and efficiently convert it into electrical energy. One widely studied approach involves using piezoelectric transducers, which generate an electrical charge in response to mechanical strain caused by vortex-induced vibrations (VIV). Although a variety of circuit architectures have been proposed for power conditioning and energy extraction, a common simplification assumes the piezoelectric element is connected to a purely resistive electrical load. This model enables straightforward estimation of power output and has been extensively used in theoretical and experimental studies.[11,23,40] Under these assumptions, the optimal electrical power harvested from the system is given by

$$P_{piezo,opt} = \frac{\omega \theta_{piezo}^2 Y^2}{2C_{piezo}}, \tag{10}$$

where θ_{piezo} is the electromechanical coupling parameter and C_{piezo} is the piezo capacitance.

The dimensionless electrical power harvested from the system ($P^*_{piezo,\,opt}$) can then be calculated using the following expression derived in Ref. 23:

$$P^*_{piezo,\,opt} = P_{piezo,opt} \frac{C_{piezo}}{\omega_n \theta_{piezo}^2 D^2} = \frac{1}{2}\left(\frac{Y}{D}\right)^2 \left(\frac{\omega}{\omega_n}\right). \tag{11}$$

In the lock-in regime—typical for structures oscillating in air—the vortex shedding frequency matches the natural frequency of the structure.[5] Under this resonance condition, Eq. (11) simplifies to

$$P^*_{piezo,\,opt} = \frac{1}{2}\left(\frac{Y}{D}\right)^2. \tag{12}$$

This relationship clearly shows that the power output scales with the square of the amplitude ratio. As a result, even moderate increases in vibration amplitude can lead to substantial gains in harvested power.

Therefore, an accurate characterization of VIV behavior must account for both the system's displacement response and the evolution of the fluid forcing, particularly the phase angle between lift force and motion and the amplitude of force fluctuations. These factors govern the amount of usable energy transferred to the structure. This underscores the importance of strategies, such as geometric modifications or flow control devices by using endplates, which can enhance the force response and extend or intensify the lock-in regime. A better understanding of these interactions is essential for developing more effective and efficient VIV-based energy harvesting systems.

III. MATERIALS AND METHODS

The experimental setup used in this study is illustrated schematically in Fig. 2. It supports two configurations: one with the cylinder rigidly mounted (stationary case) and another with the cylinder flexibly mounted, allowing vibration in the cross-flow direction.

In the stationary configuration, rigid clamps were used to secure the cylinder while enabling independent attachment and replacement of endplates.

In the flexible mounting configuration, the cylinder is attached to two elastic cantilever beams—one at the top and one at the bottom—while the opposite ends of the beams are clamped to a rigid frame.[23] This arrangement enables controlled oscillations of the cylinder in the cross-flow direction, driven by airflow. The supporting cantilever beams are made of aluminum with the following properties: a density of $\rho_b = 2730\,\text{kg/m}^3$, an elastic modulus of $E = 69\,\text{GPa}$, a width of $b_b = 25.4\,\text{mm}$, a thickness of $t_b = 3.0\,\text{mm}$, and a length of $l_b = 406\,\text{mm}$.

To explore energy harvesting under realistic operating conditions, the experimental setup was specifically designed to target an airflow velocity range of 1–4 m/s. This range reflects the typical wind speeds encountered in both outdoor and indoor environments where small-scale VIV energy harvesters are likely to be deployed, such as building ventilation systems, roadside infrastructure, or low-speed ambient wind environments.[23] The mechanical properties of the oscillator were carefully selected to ensure that the lock-in region would fall entirely within this velocity window. By aligning the onset and duration of VIV with this practical range, the study enables direct assessment of the fluid-structure interaction and energy harvesting potential under realistic flow conditions. This design choice ensures the relevance of the results to real-world applications and facilitates the development of scalable, low-cost energy harvesters capable of operating effectively in low-speed flows.

A strain gauge was bonded near the clamped end of one of the aluminum beams [Fig. 2(b)] to measure the strain resulting from the cylinder's motion. Calibration was performed to establish a precise relationship between the strain gauge output (in volts) and the tip displacement of the beam (in millimeters). This process also provided the static stiffness of the system, which is essential for calculating the natural frequency of the harvester.

The strain gauge was connected to a strain indicator (Model MM120-001469, Micro-Measurements Inc.), and the signal was acquired using a National Instruments NI-6008 data acquisition card, interfaced with MATLAB at a sampling rate of 1000 Hz.

The cylinder, fabricated using 3D printing technology with PLA plastic filament, has a diameter of $D = 80\,\text{mm}$ and a length of $L = 640\,\text{mm}$. PLA was chosen for its lightweight and rigidity, ensuring structural stability while minimizing mass. The cylinder details are shown in Fig. 3(a).

Pressure measurements were acquired using 12 probes evenly distributed around the midsection of the cylinder, following the commonly adopted configuration described by Norberg.[4] This arrangement provides adequate resolution to capture key features of the pressure distribution, including the stagnation point, flow attachment, and separation zones.

In the present study, the pressure probes were distributed uniformly around the cylinder's circumference, with probe #1 aligned with the incoming flow and probes #2 through #12 positioned clockwise at 30° intervals [Fig. 3(b)].

Flexible pressure tubing (1.5 mm inside diameter) connected the probes to a DSA5000 pressure scanner with an integrated data acquisition system. The tubing was routed through the hollow body of the cylinder and supported by brackets along the beams to minimize motion interference (Figs. 3 and 4). The pressure data were sampled at 1000 Hz and synchronized with the strain gauge readings to ensure accurate phase and frequency analysis.

The experiments for this study were conducted in the Large-scale Atmospheric Wind Tunnel facility at the City College of New York (Fig. 4). This open-circuit, suction-type wind tunnel is driven by a 20 b.h.p. electric motor with precise speed control, capable of

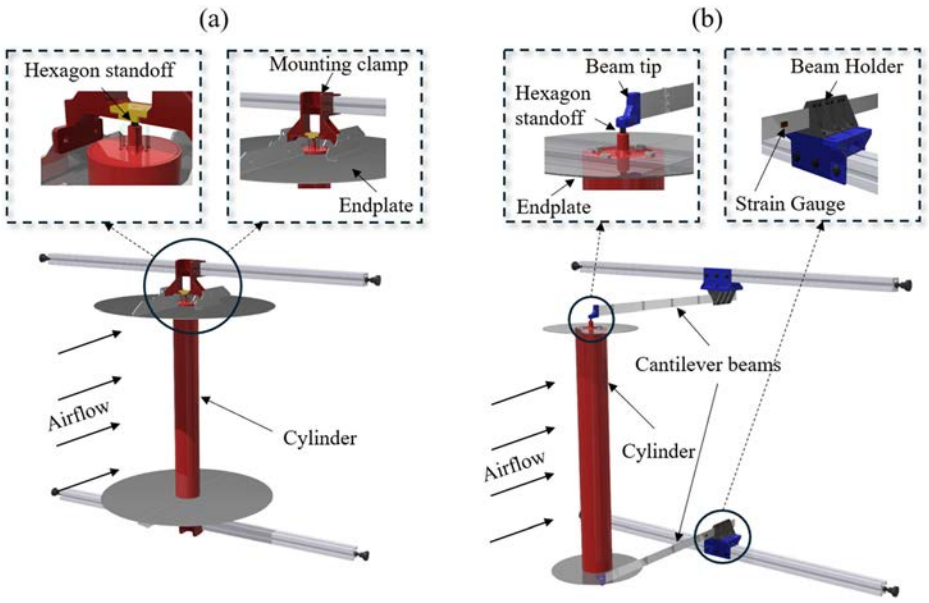

FIG. 2. Experimental setup: (a) rigidly mounted cylinder (stationary case); (b) flexibly mounted cylinder (vibrating case).

delivering free-stream velocities of up to 15 m/s within the test section. The experimental setup was placed 7 m from the entrance of the 8.4-m-long test section, ensuring uniform flow conditions. The wind tunnel features a square cross-sectional area of $1.2 \times 1.2\ m^2$, with transparent side walls and a top viewport that facilitate flow visualization. The contraction inlet is fitted with a honeycomb mesh followed by three layers of fine steel screens, producing a nearly uniform flow with turbulence intensity of less than 0.1% at the maximum speed in the test section.[41] The model blockage ratio, defined as the model frontal area divided by the wind tunnel test-section area, is 3.5%. This value lies well below commonly accepted threshold ($\approx$ 10%), which is recommended to avoid noticeable flow distortions and ensure accurate and reliable aerodynamic testing in subsonic wind tunnels.[42]

For flow visualization, a high-speed NOVA R3-4K camera, combined with Photron FASTCAM Viewer (PFV4) software, was used to record high-resolution images (4096×2304 pixels) at 500 frames per second. Illumination was provided by a DHOM-H-532–1000 laser emitting a bright green beam, with intensity controlled by a DC power supply adjustable from 0 to 5 V. To enhance visualization, a Magnum 1200 fog generator, operating with JEM PRO-FOG fluid, was used to produce dense vapor droplets.

In the stationary cylinder case, experiments were conducted to investigate the effects of endplates on the surface pressure distribution, including both pressure magnitude and frequency content. Five configurations were tested: (i) a cylinder without endplates, and (ii)–(v) with four different circular endplate designs of varying diameters. The schematic representations of these endplate configurations are shown in

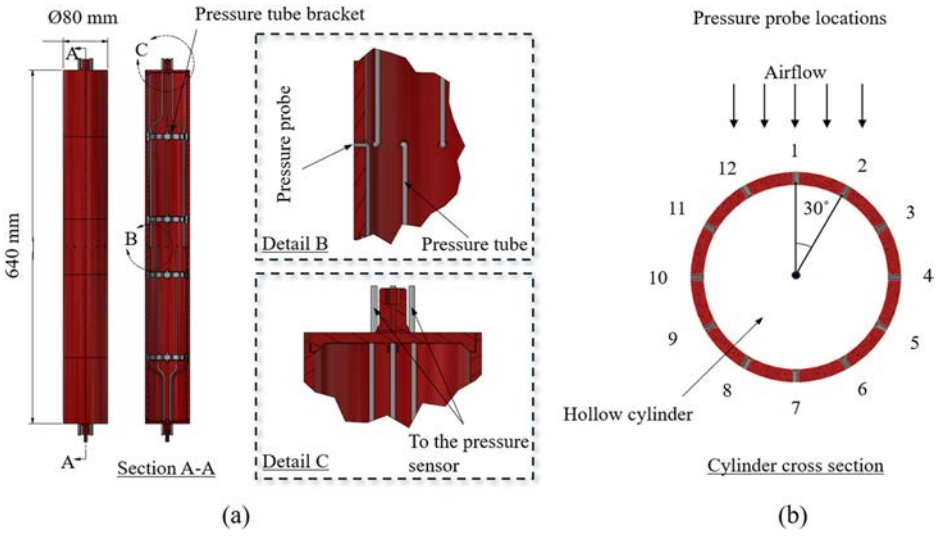

FIG. 3. The cylinder details: (a) detailed drawing and (b) probe location schematic.

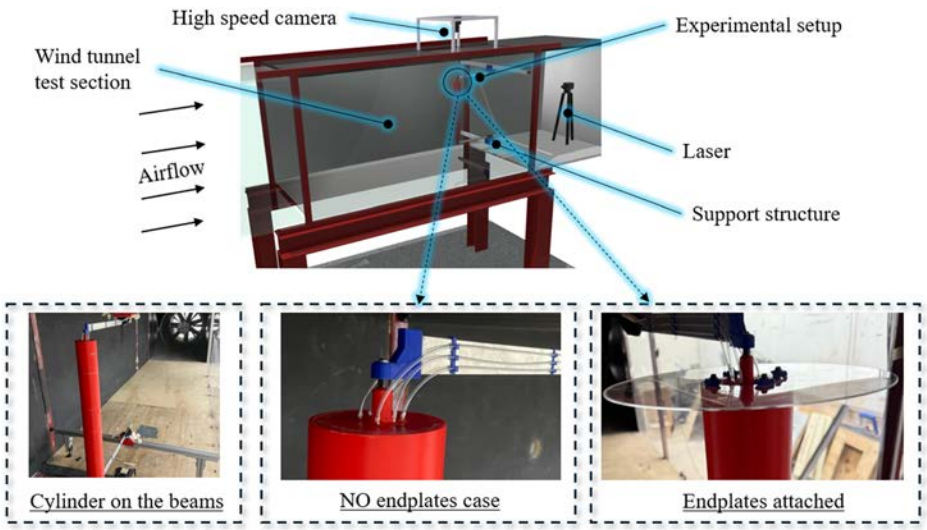

FIG. 4. Experimental setup in the wind tunnel (flexibly mounted cylinder configuration).

Fig. 5(a). The stationary case results served as a reference for interpreting flow behavior, force generation, and end-effect mitigation in the subsequent VIV experiments.

In the vibrating cylinder case, the synchronized measurement of cylinder displacement and surface pressure were used to compute lift and drag coefficients and to assess the dynamic response such as vibration amplitude, oscillation frequency, and phase lag of the system, with a focus on how the three-dimensional effects of the oscillator can be modulated by the endplates. The selection of endplate sizes for the vibrating case [Fig. 5(b)] is discussed and justified later in the paper, based on the outcomes of the stationary cylinder experiments.

Given the strong dependence of the vibration response on the system mass ratio,[7,23] polymethyl methacrylate (PMMA), a transparent thermoplastic with a relatively low density of approximately 1200 kg/m^3, was selected as the endplate material for the vibrating case. The 2D and 3D stationary tests were conducted with the same PMMA endplates used in the VIV experiments to ensure consistency between stationary and dynamic measurements. Aluminum endplates were employed only for the largest stationary spans (3.5 and 7 D) to ensure adequate rigidity of the large-diameter plates; these aluminum cases were not used in the vibrating tests. The relatively low density of PMMA helps maintain a lower mass ratio, which, as previously mentioned, increases both the maximum VIV amplitude and the vibration bandwidth. In addition, PMMA's optical transparency allows for flow visualization near the cylinder surface. The endplates were attached to the top and bottom ends of the cylinder. Endplate masses were measured, and the effect on the oscillator inertia was quantified via free-vibration tests.

IV. RESULTS AND DISCUSSION

This section presents the experimental findings and analysis of the aerodynamic loading and dynamic response of a finite-length circular cylinder with and without endplates. The results are divided into two parts according to the mounting configuration: the stationary cylinder case and the vibrating cylinder case. For the stationary configuration, the analysis focuses on surface pressure distribution and derived force coefficients under different endplate conditions. In the vibrating case, additional attention is given to vibration amplitude, frequency, and phase dynamics associated with vortex-induced vibration (VIV).

The lift and drag forces acting on the cylinder were determined from surface pressure measurements taken at 12 circumferential locations along the mid-span of the cylinder. To obtain a continuous pressure profile around the cylinder, the discrete pressure values were interpolated using a spline interpolation method.

The pressure distribution $p(\theta)$ along the cylinder surface was then integrated numerically over the full circumference ($\theta = 0$ to 2π) to calculate the total force, which was then decomposed into the

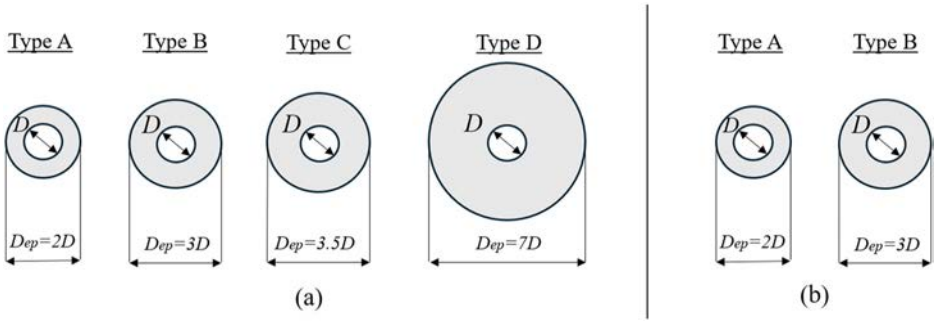

FIG. 5. Schematics of endplate geometries: (a) Stationary cylinder case. (b) Vibrating cylinder case.

streamwise and cross-flow components, corresponding to the drag force F_D and lift force F_L, respectively,

$$F_D = \frac{DL}{2}\int_0^{2\pi} p(\theta)\cos(\theta)d\theta, \quad (13)$$

$$F_L = \frac{DL}{2}\int_0^{2\pi} p(\theta)\sin(\theta)d\theta, \quad (14)$$

where D is the cylinder diameter, L is the cylinder length, θ is the angular position around the circumference (0° at the front stagnation point), and $p(\theta)$ is the surface pressure.

The influence of endplate size on both the aerodynamic forces and the structural response is examined. The outcomes from the stationary cylinder experiments serve as a baseline to understand the flow modifications introduced by endplates, which in turn inform the interpretation of the dynamic response observed in the vibrating cylinder configuration.

Stationary-cylinder measurements were performed over the velocity range relevant to the VIV tests (1.5–4.0 m/s) to establish how endplates modify the steady and unsteady aerodynamic forcing. The main conclusions are: endplates exert little influence on the upwind pressure distribution but markedly increase the downwind suction; increasing endplate span progressively amplifies this effect up to roughly 3D, beyond which further enlargement produces negligible change. Consistent with the C_p trends, the mean drag coefficient rises from 0.807 (no endplates) to ≈1.15 for spans ≥3D, the RMS lift increases from 0.048 to > 0.18 for the larger spans, and the Strouhal number increases from ≈ 0.183 to the range of 0.202–0.215. Reported C_p values are time-averaged at each pressure tap (60 s records sampled at 1000 Hz); the drag coefficient is likewise computed from time-averaged drag records, while RMS, spectral, and other derived quantities are obtained from the same time-resolved datasets. These stationary results—summarized in Appendix (Fig. 17, Table I)—guided the selection of endplate sizes for the vibrating tests.

For the flexible-mount cylinder study, three configurations were selected to represent distinct wake-modification regimes: the no-endplate case as the baseline, 2D-sized endplates as an intermediate case, and 3D-sized endplates as a fully saturated case. This selection was guided directly by the stationary-cylinder results, which showed that endplates of span ≃3D or greater produced C_p, C_D, $C_{L,}$ and wake signatures that were effectively indistinguishable from one another. Consequently, the 3.5 and 7 D spans were omitted from the vibrating tests because their dynamic response was expected to lie within the same regime represented by the 3D case. In addition, increasing endplate diameter substantially raises the structural mass attached to the oscillator, which tends to reduce the vibration amplitude and narrow the lock-in envelope. Because maximizing amplitude and lock-in bandwidth is important for the planned flexible-mount study (and for potential energy-harvesting applications), the 3D endplate was selected as the representative "saturated" case to avoid the mass penalty associated with larger plates.

In this study, a series of static load tests (i.e., eighteen tests with different loadings) were performed to determine the system's static stiffness, which was found to be $k = 308.9$ N/m. In addition, free vibration tests were carried out for each oscillator configuration to determine the system's natural frequency and the structural damping ratio. With both the stiffness and natural frequency determined experimentally, the total vibrating mass could be verified using the relationship $m = \frac{k}{(2\pi f_n)^2}$.

A baseline test was conducted using a bare cylinder (i.e., no-endplate) to establish a reference for evaluating the typical behavior of the oscillator. The vibrating mass in this configuration was measured to be $m = 0.403$ kg ($m^* = 105$). A free vibration test conducted for this setup yielded a natural frequency of f_n=4.41 Hz and a damping ratio of ζ between 0.3% and 0.32%. It was determined that the air velocity range from 1.5 to 3.5 m/s fully encompasses the lock-in region of the system. To capture the pre-lock-in and post-lock-in behavior, the range was extended to 1.0–4.0 m/s, corresponding to a Reynolds number range of approximately 5300 to 21 200, based on the cylinder diameter (i.e., $D = 80$ mm) under standard atmospheric conditions.

During wind tunnel testing, the free-stream velocity was increased in 0.02 m/s increments, allowing the oscillator to reach steady-state at each step before data acquisition. The time required to stabilize the response was estimated from the measured damping ratio and natural frequency using the decay-time constant $\frac{1}{\zeta\omega_n}$, which gave an order-of-magnitude estimate of ≈ 60 s; a conservative waiting period of 120 s was, therefore, employed at each velocity step to ensure full stabilization. Steady-state was verified by examining the vibration-amplitude envelope over roughly 250 cycles: the amplitude time series showed no systematic increasing or decreasing trend (assessed via a linear trend test on the peak-amplitude envelope). Once steady-state was achieved, strain gauge and pressure data were recorded over a 60-s interval, corresponding to approximately 250 vibration cycles.

The oscillator exhibits the following behavior (Fig. 6): At low air velocities, no noticeable vibrations occur, corresponding to the pre-lock-in regime. When the reduced velocity $U^* = \frac{U_\infty}{f_n D}$ reaches $U^* = 5.24$, vibrations initiate, marking the beginning of the "initial branch" of the lock-in regime. A further increase in air velocity leads to an almost linear growth in the vibration amplitude. The amplitude peaks at 37.6 mm (amplitude ratio $A^* = \frac{Y}{D} = 0.47$) at a reduced velocity of $U^* = 7.14$.

Beyond this peak, a sharp drop in vibration amplitude is observed, marking the transition of the system into the "lower branch" of the lock-in regime. As air velocity continues to increase, the vibration amplitude decreases with a smoother slope compared to the rapid amplitude growth observed in the initial branch. Finally, vibration cessation is observed at a reduced velocity of $U^* = 9.87$, signaling the system's entry into the post-lock-in region.

For validation, the present response is compared with a closely related experimental case in Ref. 10 (cylinder D = 75 mm, aspect ratio 9, mass-damping parameter $m^*\zeta = 0.360$); the test in Ref. 10 shows vibration onset at U^*≃5–5.5, a peak amplitude A^*=0.40, and the end of the lock-in region near U^*≃9. The present case ($D = 80$ mm, aspect ratio 8, $m^*\zeta = 0.336$), therefore, exhibits very similar behavior: onset at $U^* \simeq 5.2$, a slightly larger peak amplitude A^*=0.47, and a marginally later termination of lock-in at U^*≃10. These small differences are consistent with the slightly lower mass-damping in the present study (which tends to increase peak amplitude and broaden the lock-in range) and minor geometric differences in diameter and aspect ratio. An additional case reported in Ref. 10 with $m^*\zeta = 0.255$ produced A^*= 0.53 and a slightly later lock-in termination, supporting the established dependence of peak amplitude and lock-in bandwidth on mass-damping.[8,23,43,44] Taken together, the close quantitative agreement with Ref. 10—and the consistent trend with mass-damping reported

in Refs. 8, 23, 43, and 44—supports the accuracy of the present measurements.

To isolate the aerodynamic effects of endplates from the influence of added mass, two sets of experiments were designed. Since the addition of endplates increases the total vibrating mass—and consequently the mass ratio m^* of the oscillator—it was necessary to account for this change to accurately assess the impact on VIV behavior.

The first set of experiments (2D-sized endplates set: $m = 0.463$ kg, $m^* = 121$, $f_n = 4.11$ Hz, $\zeta = 0.3\%$) included two configurations: (i) the oscillator equipped with 2D-sized endplates, and (ii) the bare cylinder (without endplates) with added weights to match the total vibrating mass of the 2D-sized endplates case.

The second set of experiments involved three configurations designed to match the total mass of the system with 3D-sized endplates ($m = 0.558$ kg, $m^* = 146$, $f_n = 3.74$ Hz, damping ratio $\zeta = 0.3\%$): (i) the oscillator with 3D-sized endplates, (ii) the oscillator with 2D-sized endplates and additional weight to match the mass of the 3D-sized endplates case, and (iii) the bare cylinder with added weight to again match the 3D-sized endplates configuration. This approach ensured that any observed differences in response could be attributed to aerodynamic effects of the endplates rather than variations in inertial properties.

The results of the two experimental sets are presented in Fig. 8, which shows the amplitude response of the oscillator plotted against the reduced velocity for all tested configurations. The amplitude response for the first experimental set—comparing the oscillator with 2D-sized endplates and the bare cylinder with matched vibrating mass—is presented in Fig. 7(a). At low air velocities, no vibration was observed for either configuration. Oscillations initiated at a reduced velocity of $U^* = 5.4$ in both cases, indicating the onset of the lock-in regime. Under resonance conditions, where the vortex shedding frequency equals the natural frequency of the system, this transition corresponds to a Strouhal number of approximately $St = 0.184$. Following the onset of lock-in, both configurations exhibited a sharp, quasi-linear

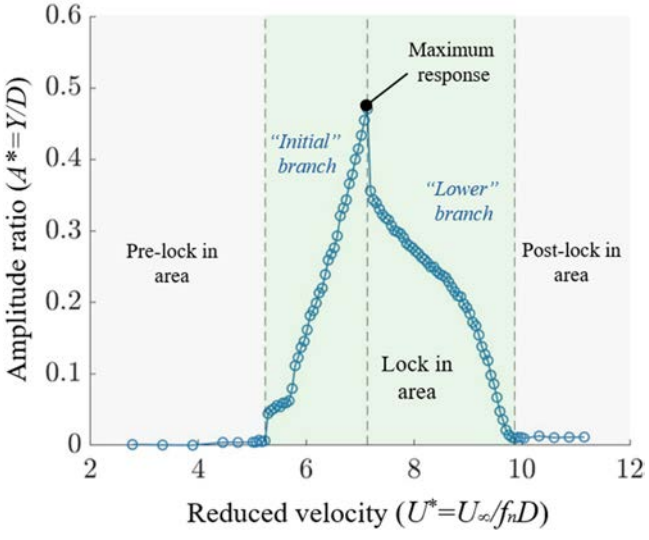

FIG. 6. Amplitude response of the bare cylinder oscillator as a function of reduced velocity ($m*$=105, $\zeta = 0.32\%$).

increase in vibration amplitude with increasing air velocity. The initial slopes of the amplitude response curves were nearly identical. However, once the amplitude ratio exceeded approximately 0.3, the curves diverged—with the 2D-sized endplates configuration showing a steeper slope, suggesting enhanced aerodynamic forcing. The oscillator with 2D-sized endplates reached a slightly higher peak amplitude compared to the no-endplate case. Moreover, the peak response occurred at slightly lower reduced velocity for the 2D-sized endplate configuration, i.e., $U^* = 7.1$, compared to $U^* = 7.3$ for the bare cylinder case. Beyond the peak, both systems exhibited a sharp drop in vibration amplitude, indicating the transition to the lower branch of the VIV response. The response curves converged again around amplitude ratio of 0.2 (at $U^* = 8.6$), and the lock-in regime concluded at approximately $U^* = 9.6$ for both cases. A further increase in air velocity did not result in significant oscillations, confirming the transition to the post-lock-in regime.

Figure 7(b) shows the results from the second experimental set, which includes the oscillator with 3D-sized endplates, as well as the 2D-sized endplates and bare cylinder configurations, each supplemented with added mass to match the total mass of the 3D-sized endplates configuration. The overall system behavior closely followed the trends observed in the first set. Vibration onset occurred at a reduced velocity of $U^* = 5.5$, corresponding to a Strouhal number of approximately $St = 0.182$, marking the beginning of the lock-in regime for all three configurations. Following the onset of oscillations, all configurations exhibited a sharp, quasi-linear increase in vibration amplitude with increasing air velocity. However, the 3D-sized endplates case transitioned to the lower branch earlier, i.e., at approximately $U^* = 6.3$, while the 2D-sized endplates and no-endplate configurations continued their upward trends. Between these two, the 2D-sized endplates configuration demonstrated a steeper slope, suggesting enhanced aerodynamic forcing compared to the bare cylinder. The peak amplitude occurred at $U^* = 6.8$ for the 2D-sized endplates case and at $U^* = 7.2$ for the no-endplate configuration. After the peak, both the 2D-sized endplates and bare cylinder cases exhibited a sharp drop in amplitude, indicating transition to the lower branch. In contrast, the 3D-sized endplates configuration followed a smoother evolution within the lower branch, without a distinct amplitude drop. Eventually, all three configurations converged at an amplitude ratio of approximately 0.15 in the lower branch. As the reduced velocity exceeded $U^* = 9.2$, the system exited the lock-in regime and entered the post-lock-in region where oscillations diminished significantly.

The experimental results demonstrate that the presence of endplates does not influence the onset or termination of vortex-induced vibration. This indicates that the addition of endplates has a negligible effect on the vibration bandwidth, as all configurations exhibited the same initiation and cutoff velocities. Differences become apparent starting in the initial branch of the amplitude response, particularly beyond an amplitude ratio of approximately 0.3. These differences persist through the peak response and into the lower branch, where they gradually diminish and become negligible around an amplitude ratio of 0.15–0.2.

The peak amplitude responses A^*_{peak} of the studied oscillators are plotted against the mass-damping parameter $(m^* + C_A)\zeta$ in Fig. 8(a), along with comparative datasets from Refs. 7 and 23. Here, C_A represents the ideal added mass coefficient, which is equal to 1.0 for a circular cylinder oscillating transversely in an ideal, incompressible fluid.[12]

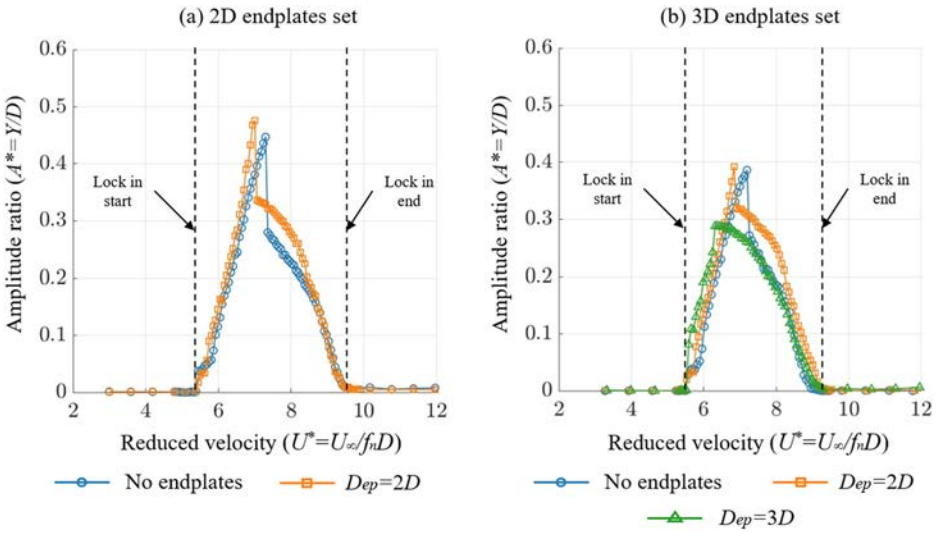

FIG. 7. Amplitude response of the cylinder oscillator as a function of reduced velocity with varying endplates configurations: (a) 2D-sized endplates set ($m^* = 121$, $\zeta = 0.3\%$). (b) 3D-sized endplates set ($m^* = 146$, $\zeta = 0.3\%$).

The dataset from Ref. 23 was obtained using the same wind tunnel and harvester configuration as the present study, but explored a broader range of system parameters, including varying masses, stiffnesses, and cylinder diameters.

A comparison of the bare cylinder configurations revealed that a lower system mass leads to a higher peak amplitude of vibration, consistent with the findings of Ref. 23. Specifically, the bare cylinder without added mass (m^*=105) had a peak amplitude ratio of $A^*_{peak} = 0.47$, while for the same cylinder with added mass matching the 2D-sized endplates configuration (m^*=121) had $A^*_{peak} = 0.45$, and with mass matching the 3D-sized endplates configuration (m^*=146) A^*_{peak} dropped to 0.39. The same cylinder equipped with 2D-sized endplates (m^*=121) and 3D-sized endplates (m^*=146) had peak amplitudes of A^*_{peak}=0.48 and A^*_{peak}=0.29, respectively. These results highlight that the 2D endplates slightly enhance the peak amplitude despite their added mass, whereas the 3D endplates shift and reshape the lock-in response so that the global maximum is smaller.

To assess the implications for energy harvesting, Fig. 8(b) presents the optimal dimensionless harvested power at peak vibration, computed using Eq. (11) from the measured peak amplitudes. As shown in Fig. 8(b), the 2D endplate cases tend to increase the optimal harvested power: notably, the 2D case (m^*=121) produces higher dimensionless power at peak amplitude than the lighter bare-cylinder configuration (m^*=105) without endplates. Thus, the aerodynamic benefit of the 2D endplates is sufficient to overcome the associated mass penalty in terms of optimal harvested power, consistent with the peak-amplitude trends. These results underline that the net effect of endplates on energy harvesting depends on the balance between increased aerodynamic forcing and the added inertia they introduce.

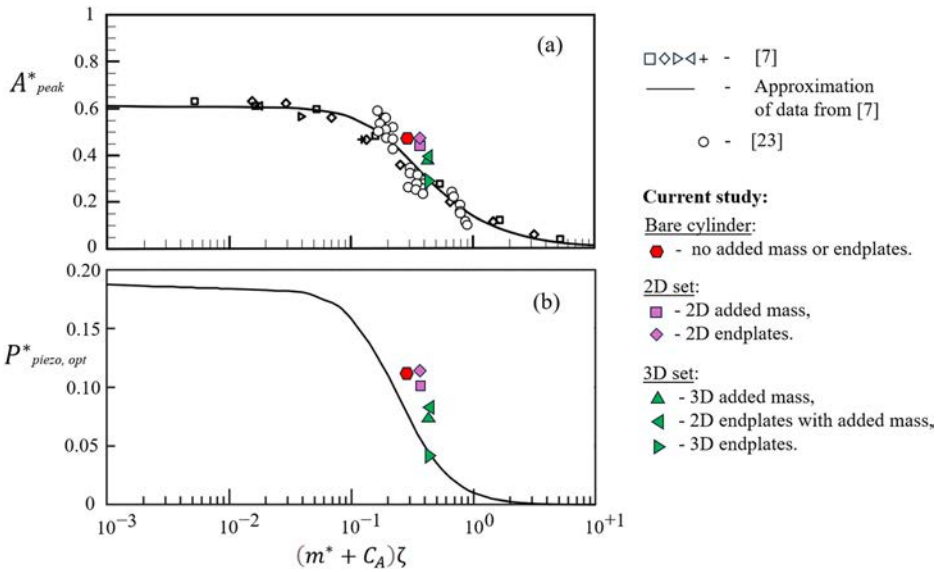

FIG. 8. Peak-amplitude data vs mass-damping parameter. Symbols compile experimental results from Refs. 7 and 23; the black solid line is an approximation of the data from Ref. 7; filled markers indicate the present-study cases: bare cylinder (m^*=105, $\zeta = 0.32\%$); 2D-sized endplates set (m^*=121, $\zeta = 0.3\%$); 3D-sized endplates set (m^*=146, $\zeta = 0.3\%$). Peak amplitude ratio; (b) optimal dimensionless harvested power at peak vibration.

To better understand the influence of endplates on the aerodynamic loading of a vibrating cylinder, a detailed force analysis (for the 3D endplates set) was conducted based on time-resolved surface pressure measurements. The analysis focuses on the behavior of the pressure-induced forces across three distinct regimes: pre-lock-in, lock-in, and post-lock-in. These regimes represent key stages in the vortex-induced vibration (VIV) response, where the nature of fluid-structure interaction evolves with air velocity. In each regime, the lift and drag forces, as well as their temporal characteristics and phase relationships, are examined to reveal how different endplate configurations modify the underlying flow mechanisms and dynamic forcing on the structure.

A. Pre-lock-in regime

In the pre-lock-in regime, the surface pressure distribution of the flexibly-mounted cylinder differs notably from that observed in the fixed cylinder cases. Figure 9(a) presents the circumferential pressure coefficient C_p for four configurations: a fixed bare cylinder, a fixed cylinder with 3*D*-sized endplates, a flexibly mounted bare cylinder, and a flexibly mounted cylinder with 3*D*-sized endplates. The results demonstrate that, in the absence of endplates, the flexibly mounted cylinder (i.e., free to vibrate) experiences a reduced pressure force compared to the fixed cylinder (i.e., constrained from vibrating). Specifically, the peak magnitude of the negative C_p values at the suction surface was reduced by 50%, i.e., from approximately $C_p = -1.0$ in the fixed bare cylinder to about $C_p = -0.5$ in the flexibly mounted bare cylinder configuration. In contrast, the addition of endplates (of 3*D*-sized) leads to an even more evident pressure force reduction, i.e., the peak magnitude of the suction pressure coefficient dropped from approximately $C_p = -1.5$ in the fixed configuration to $C_p = -0.5$ in the flexibly-mounted case. However, it should be noted that, when the cylinder is flexibly mounted, the addition of endplates has minimal influence on the pressure distribution, as the C_p profile of the 3*D*-sized endplate configuration closely resembles that of the bare case.

Frequency analysis of the fluctuating lift force [Figs. 9(b)–9(e)] provides key insight into the pre-lock-in aerodynamic behavior. For the fixed cylinders, a distinct dominant frequency is observed in the lift signal, corresponding to $St = 0.18$ for the bare cylinder and $St = 0.21$ for the cylinder with endplates. Moreover, the power spectral density (PSD) magnitude for the endplate case is nearly an order of magnitude higher, indicating significantly stronger unsteady aerodynamic loading. In contrast, the flexibly mounted cylinder exhibits no distinct frequency peak in either configuration, confirming the absence of periodical vortex shedding and suggesting that the structural vibrations disrupt the coherence of the wake, thereby suppressing organized shedding behavior.

The suppression of vortex shedding in the flexible cases is also evidenced by the pressure distributions, which remain nearly identical regardless of the presence of the endplates. Additionally, the pressure fluctuations are minimal, close to the noise level, indicating a lack of organized unsteady flow structures. The mean drag coefficient for the flexibly mounted cylinder remains consistently low at $C_D^{mean} = 0.64$ across all configurations. In comparison, the fixed bare cylinder exhibits a higher value of $C_D^{mean} = 0.81$, while the fixed cylinder with the 3D-sized endplates reaches $C_D^{mean} = 1.14$. Similarly, the RMS of the lift coefficient C_L^{RMS} is close to zero in all flexibly mounted cases, confirming the absence of periodic transverse forcing. In contrast, the fixed cylinder with endplates exhibits significantly elevated lift fluctuations, consistent with the strong periodic vortex shedding observed in the spectral data.

Together, these results demonstrate that structural flexibility plays a dominant role in suppressing vortex formation, unsteady aerodynamic forces, lift and drag in the pre-lock-in regime. Under such conditions, the addition of the endplates has minimal influence, as their aerodynamic effects are outweighed by the cylinder's dynamic response to the flow.

B. Lock-in regime

As the flow velocity increases, the system transitions from the pre-lock-in-state into the lock-in regime, where the vortex shedding frequency synchronizes with the natural frequency of the structure. In this regime, a strong coupling develops between the fluid forces and the structural motion, leading to large-amplitude oscillations and significant changes in the aerodynamic loading. Unlike the pre-lock-in regime, where the influence of endplates on flexible configurations is minimal, the lock-in phase reveals more pronounced differences across the tested configurations, both in terms of pressure distribution and aerodynamic forces.

The variations of amplitude ratio, drag, and lift coefficients throughout the pre-lock-in, lock-in, and post-lock-in regime for the three configurations of the 3D-sized endplates experimental set ($m^* = 146$, $f_n = 3.74$ Hz, $\zeta = 0.3\%$), including the bare cylinder with added mass, 2D-sized endplates with added mass, and 3D-sized endplates, are shown in Fig. 10. It presents aligned plots of the amplitude ratio, mean drag coefficient C_D^{mean}, and RMS lift coefficient C_L^{RMS}, as functions of reduced velocity for each configuration. These plots are arranged vertically to share a common x-axis, enabling direct visual comparison of the onset, peak, and decay trends across aerodynamic forces and vibration response.

Prior to the onset of lock-in, all cases exhibited similar aerodynamic behavior, with a steady drag coefficient of approximately $C_D^{mean} = 0.64$ and a low RMS lift coefficient around $C_L^{RMS} = 0.04$–0.05, reflecting a small unsteady aerodynamic loading observed in the pre-lock-in regime.

With the onset of vortex-induced vibration, both C_D^{mean} and C_L^{RMS} increased significantly. For the bare cylinder, the rise in the aerodynamic coefficients occurred gradually with increasing air velocity. In contrast, the 2D- and 3D-sized endplate configurations exhibited abrupt jumps in both C_D and C_L at the onset of vibration, with the 3D-sized endplates producing the largest vibrational response. The peak drag coefficients C_D^{mean} reached values of 0.98 (bare), 1.33 (with 2D-sized endplates), and 1.38 (with 3D-sized endplates), while the corresponding peak lift coefficients C_L^{RMS} were 0.85, 1.06, and 1.09, respectively. These results indicate that the addition of endplates significantly enhanced the unsteady aerodynamic loading during the lock-in regime.

Interestingly, despite producing the highest lift coefficient, the 3D-sized endplates configuration exhibited the lowest peak amplitude response, with $A^* = 0.29$ [see Fig. 10(c)], compared to $A^* = 0.39$ for the bare cylinder [see Fig. 10(a)]. Given that the vibrating mass remained constant across all configurations, the observed reduction in amplitude response is attributed to changes in the fluid-structure interaction, caused by the modified wake dynamics due to the spanwise flow confinement introduced by the endplates. The higher lift

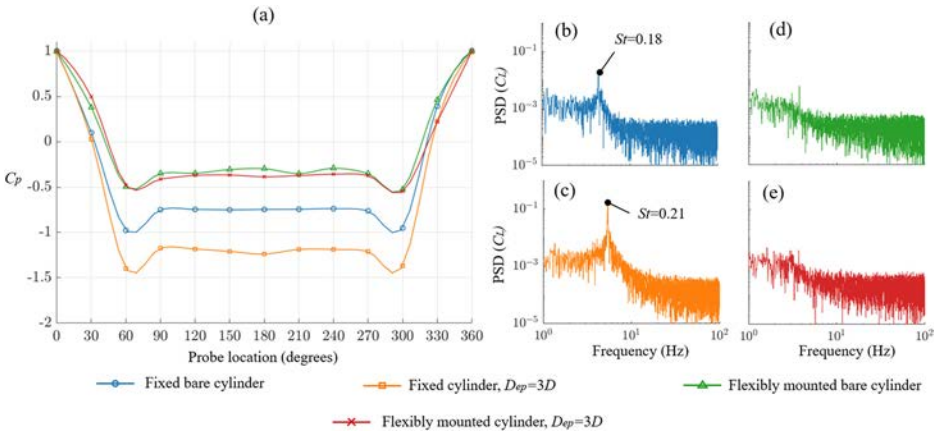

FIG. 9. Pressure coefficient distributions and frequency spectrum of the lift force (pre-lock-in): (a) pressure coefficient C_P; (b) C_L frequency spectrum of the fixed bare cylinder; (c) C_L frequency spectrum of the fixed cylinder with 3D endplates; (d) C_L frequency spectrum of the flexibly mounted bare cylinder; and (e) C_L frequency spectrum of the flexibly mounted cylinder with 3D endplates.

coefficients observed for the 3D endplate configuration must be considered alongside the fact that its peak response occurs at a different reduced velocity. The 3D case reaches a local peak of A^*=0.29 at U^*=6.3 [Fig. 10(c)]; at the same reduced velocity, the no-endplate case attains only A^*=0.19 [Fig. 10(a)]. In other words, the 3D endplates produce larger amplitudes in the initial branch for the same U^*, consistent with their higher aerodynamic forcing. Thus, endplates increase the early-stage forcing and amplitudes but also alter the initial to lower branch transition so that the maximum amplitude over the entire tested U^* range can be smaller than that of the bare cylinder.

Another notable and consistent observation across all configurations is the mismatch between the peak aerodynamic forces and the peak structural response. For the bare cylinder, the maximum vibration amplitude occurs at $U^* = 7.2$, yet this lags behind the peaks in aerodynamic forcing: C_D^{mean} peaking at $U^* = 6.9$, and C_L^{RMS} peaking even earlier at $U^* = 6.6$. The 2D-sized endplates case shows a closer alignment between the peak response and the peak drag, both occurring at $U^* = 6.8$, while the lift force still peaks slightly earlier at $U^* = 6.6$. For the configuration with the 3D-sized endplates, the drag and lift peaks occur just before the maximum amplitude response, delayed by only one velocity increment ($\approx$ 0.02 m/s), suggesting a more synchronized but constrained dynamic regime.

This sequencing behavior evidently suggests a change in wake dynamics during the transition from peak forcing to peak displacement. One plausible interpretation is a shift from a 2S (two single vortices per cycle) wake pattern to a 2P (two vortex pairs per cycle) pattern, along with the onset of the lower branch in VIV. For the bare cylinder configuration, this transition occurs after the peak aerodynamic forces, allowing a continued increase in the vibrational amplitude before entering the lower branch. In contrast, the presence of endplates, particularly the 3D-sized endplates, accelerates this transition, reducing the effective duration of the initial branch and causing earlier entry into the lower branch, despite stronger aerodynamic excitation.

These findings underscore the roles of endplates in reshaping the fluid-structure interaction of the oscillator system, not only by changing the magnitude of aerodynamic forces but also by altering the structural response. Following the peak vibration response in each configuration, both coefficients decreased as the system transitioned toward the lower branch of the response. The reduction in C_L^{RMS} was particularly significant for the configurations with endplates, with RMS lift dropping by roughly a factor of three. The drag coefficient also declined, but to a lesser extent—by about 30%. As the reduced velocity approached $U^* = 7.2$, the aerodynamic coefficient curves for all three configurations converged, sharing nearly identical values through the remainder of the lock-in regime. Notably, the C_D^{mean} and C_L^{RMS} values at the conclusion of lock-in closely matched those observed just before its onset, suggesting a symmetric aerodynamic response around the resonance zone.

Figure 11 presents the pressure fluctuation behavior, expressed as the standard deviation of the pressure coefficient, for the three studied configurations with equal mass, i.e., the bare cylinder with added mass, the cylinder with 2D-sized endplates and added mass, and the cylinder with 3D-sized endplates. For each case, two representative operating points were selected: one before the peak amplitude response [Fig. 11(a)] and one after the peak [Fig. 11(b)], corresponding to conditions within the initial and lower branches of the lock-in regime, respectively. Across all configurations, a clear trend is observed: pressure fluctuations decrease significantly, by roughly 50%, after the system passes the peak vibration amplitude. This reduction reflects a weakening of unsteady aerodynamic loading and vortex shedding intensity as the system transitions out of the initial branch.

In the pre-peak regime, the 2D- and 3D-sized endplates configurations exhibit higher standard deviations of the pressure coefficient C_p^{STD} than that of the bare-cylinder case, suggesting intensified unsteady wake behavior. This enhancement is attributed to flow confinement, which preserves coherent vortex structures by suppressing three-dimensional effects, such as the spanwise flow, typically generated at the cylinder ends. However, in the post-peak regime, the pressure fluctuations become comparable across all configurations, indicating that the influence of endplates on unsteady loading diminishes as the system settles into reduced-amplitude oscillations.

It is worth mentioning that the regions of maximum pressure fluctuation shift between regimes. In the pre-peak state, the highest C_p^{STD} values are observed at the sides of the cylinder, particularly at probes 3–4 (60°–90°) and 10–11 (270°–300°), consistent with the formation of strong, alternating single vortices. After the peak, the occurrence of these events shifts forward, with probes 2 (30°) and 12 (330°) showing the largest or similar fluctuations as probes 3–4 and 10–11, suggesting a change in the vortex formation pattern. This transition is

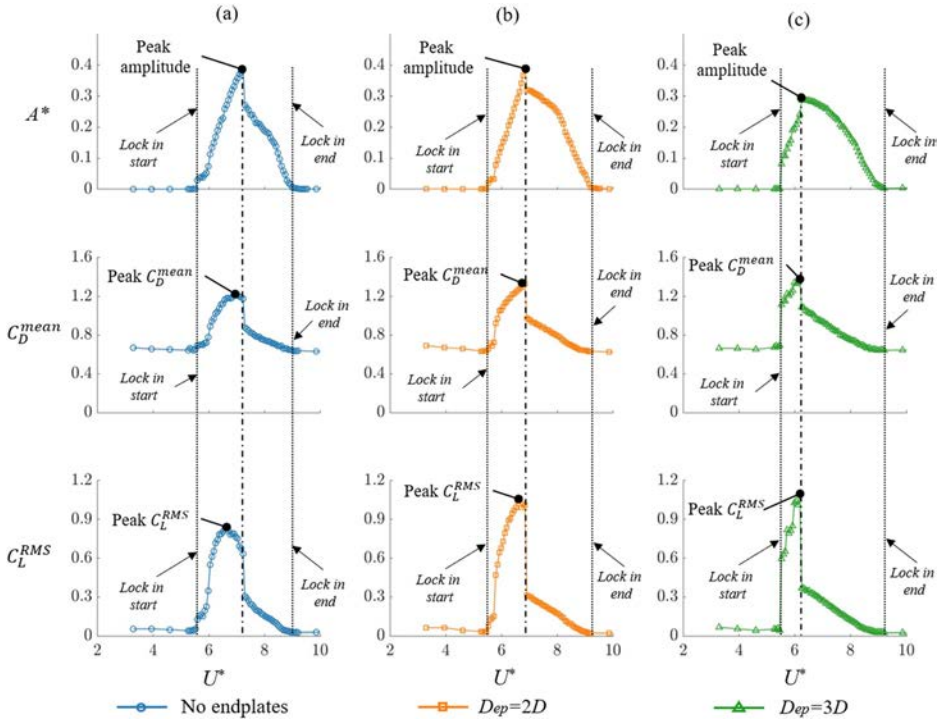

FIG. 10. Amplitude ratio, drag and lift coefficients as a function of reduced velocity for the 3D endplates experimental set (m^*=146, ζ = 0.3%): (a) No endplates; (b) D_{ep}=2D; (c) D_{ep}=3D.

likely associated with a shift from single vortex shedding to a more complex paired vortex formation, which has been reported in the literature for cylinders operating in the lower branch of VIV response.[9,23]

These findings confirm that the pre-peak amplitude state is characterized by the strongest unsteady pressure loading, particularly on the sides of the cylinder, and that the post-peak regime is marked by both a redistribution and attenuation of pressure fluctuations, aligned with the observed decay in vibration amplitude and lift force.

The evolution of the phase angle between the aerodynamic lift force and the transverse (oscillation) displacement of the cylinder is shown in Fig. 12(a) for the three studied configurations: the bare cylinder with added mass, the cylinder with 2D-sized endplates and added mass, and the cylinder with 3D-sized endplates.

The results indicate that throughout the lock-in regime, the phase angle undergoes a significant variation. At the onset of lock-in, the phase angle is slightly positive, indicating that the lift force leads the structural oscillation displacement in time. For the bare cylinder and the 2D-sized endplates configurations, the phase angle reaches values of up to 30°, while for the case of 3D-sized endplates, it is notably smaller, around 5°. As the air velocity increases and the system progresses along the initial branch, the phase angle converges to a near-constant value of approximately 5°–10° across all configurations, beginning at a $U^* = 6.1$–6.2. This small positive phase lag corresponds to positive airflow-to-structure energy transfer, providing the energy needed to initiate vibration and causing the amplitude to grow as the lock-in mechanism begins. A sharp transition in phase occurs immediately after the peak vibration amplitude, marking the entry into the lower branch. At this point, the phase angle shifts rapidly toward 180°, indicating that the lift force is nearly out of phase with the cylinder's oscillation displacement. For all configurations, the phase angle settles around 165°–170°, shortly after the peak, and continues to shift toward 180° throughout the rest of the lock-in regime. As the phase angle approaches 180°, the net energy transfer from the airflow to the structure diminishes, elucidating the declining amplitude observed in the lower branch of the lock-in regime. The phase angle behavior, particularly the observed 180° jump during transitions between initial and lower response branches, aligns closely with the findings of Khalak and Williamson.[9] Their work demonstrated similar discontinuities in phase associated with mode transitions in vortex-induced vibrations at low mass-damping.

These findings highlight that the use of endplates primarily modulates the phase behavior at the onset of the lock-in regime, which directly affects mean power input via Eq. (9). Thus, a more favorable phase (larger $\sin\varphi$) at onset can increase energy transfer only if the aerodynamic forcing is comparable. In the present data, the no-endplate case displays a phase angle that is more favorable for energy transfer than the 2D and 3D cases at onset; however, the lift amplitude for the no-endplate configuration is roughly six times smaller than for the 3D endplate case. As a result, the product $C_L\sin\varphi$—and therefore the expected mean power input—remains substantially larger for the 3D configuration despite its less favorable phase. Beyond the onset region, the phase responses converge and differences in energy input become dominated by the differing lift amplitudes rather than timing.

The evolution of the frequency ratio f^*, defined as the ratio of the oscillation frequency to the natural frequency of the system, is shown in Fig. 12(b) for the three studied configurations. Interestingly, the frequency ratio also changes throughout the lock-in regime, reflecting the dynamic coupling between the airflow and the oscillator.

At the onset of lock-in, the bare cylinder and the 2D-sized endplates configuration begin oscillating very close to their natural

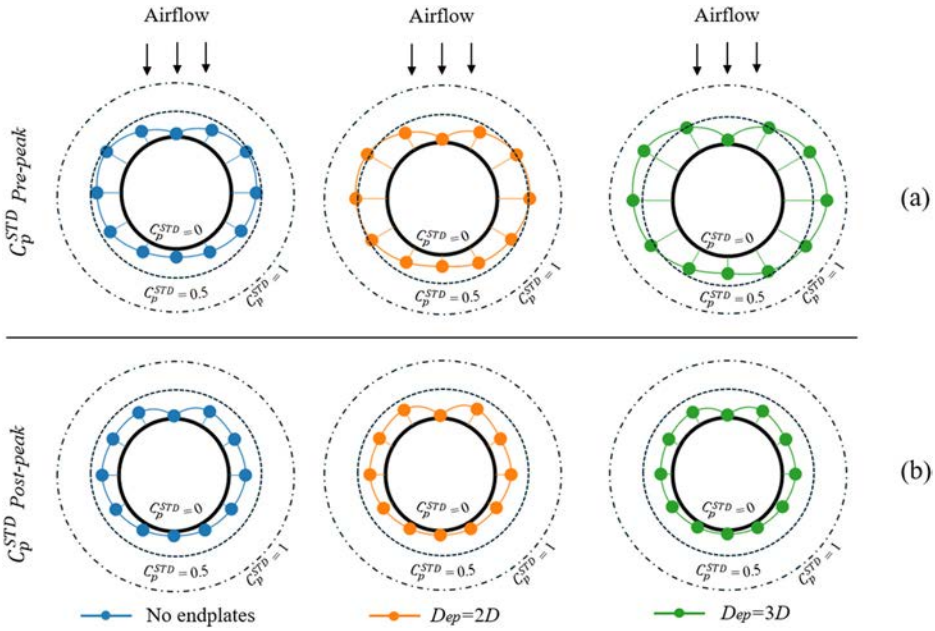

FIG. 11. Pressure coefficient STD variation in the lock-in regime at different probe locations for the 3D-sized endplates experimental set (m^*=146, ζ = 0.3%): (a) Pre-peak and (b) post-peak.

frequency, with a frequency ratio of approximately 1.00. In contrast, the 3D-sized endplate case shows a slightly lower initial value of about 0.99. Given that all other factors remain unchanged, this reduction is attributed to the complete flow confinement imposed by the larger endplates.

As the air velocity increases, all configurations converge to a frequency ratio near 0.99, which is maintained consistently through the initial branch of the lock-in regime up to the point of peak vibration amplitude. However, immediately after the peak, a noticeable shift occurs: the frequency ratio increases slightly above unity for all cases. The rise is more pronounced for the 2D- and 3D-sized endplate configurations, but by the time the system approaches the end of the lock-in regime, all configurations exhibit a frequency ratio of approximately 1.01.

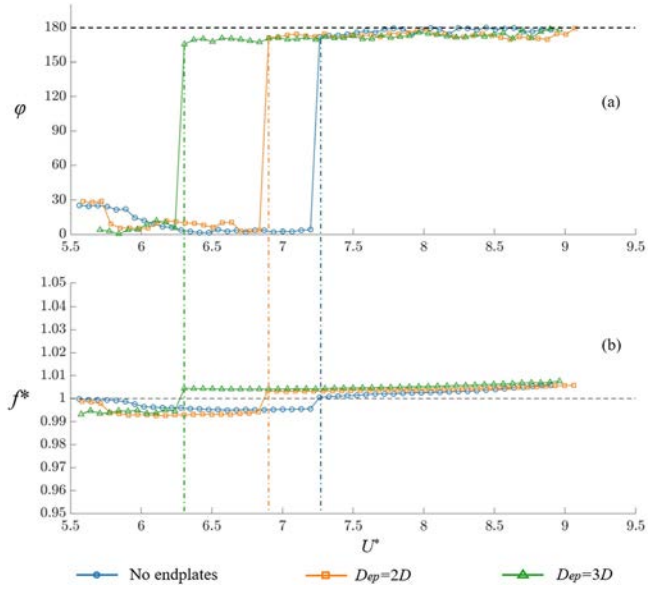

FIG. 12. Characteristics of the lock-in regime for the 3D endplates experimental set (m^*=146, ζ = 0.3%): (a) Phase angle. (b) Frequency ratio.

This behavior parallels the low-mass-ratio cylinder tests of Khalak and Williamson,[8] who observed that the nondimensional oscillation frequency deviates slowly from unity as the reduced velocity increases, reflecting the evolving coupling between body motion and wake vortex dynamics rather than pure structural resonance.

While the vibration frequency ratio varies very slightly (i.e., from 0.99 to 1.01, corresponding to an absolute change of ±0.037 Hz around the 3.74 Hz natural frequency of the 3D-sized endplates experimental set configurations), this shift still exceeds the ±0.014 Hz uncertainty imposed by the 1 ms sampling interval by more than a factor of two, confirming that the observed ratio change is trustworthy and not due to measurement resolution limitations.

This behavior indicates that the transition from the initial to the lower branch is not only marked by abrupt changes in aerodynamic loading and phase angle, but also by a subtle but measurable variation in vibration frequency.

C. Post-lock-in regime

As the reduced velocity increases beyond the lock-in region, the system transitions into the post-lock-in regime, where the vortex shedding frequency is no longer synchronized with the natural frequency of the structure. The aerodynamic behavior of the system in the post-lock-in regime reveals distinct differences between the studied configurations, particularly in how the wake develops once structural oscillations subside. The pressure coefficient distributions, shown in Fig. 13(a), indicate that the bare cylinder and the 2D-sized endplate configurations exhibit nearly identical C_p profiles in this regime. Both

cases show a minimum pressure coefficient of approximately $C_p = -0.5$ on the cylinder sides, closely matching the values observed during the pre-lock-in regime. The observed similarity can be attributed to the fact that the 2D-sized endplates, despite being attached at the cylinder ends, only alter the flow in the immediate tip regions. As a result, the mid-span section, where the pressure taps are located, remains largely unaffected, yielding pressure distributions that closely align with the bare-cylinder case.

In contrast, the 3D-sized endplates configuration exhibits a markedly different pressure distribution. The minimum C_p value drops to around -0.75, indicating a stronger suction region on the cylinder sides. This enhanced pressure differential suggests that 3D-sized endplates promote more intense vortex dynamics in the wake, even in the absence of significant cylinder motion.

The drag coefficient further reinforces this trend. For both the bare cylinder and the 2D-sized endplates configurations, the drag coefficient stabilizes around $C_D^{mean} = 0.64$, consistent with the values observed in the pre-lock-in regime. However, the 3D-sized endplates configuration maintains an elevated drag coefficient of $C_D^{mean} = 0.92$, reflecting a stronger base suction and more persistent vortex structures in the wake.

The spectral analysis of the lift-force signal was performed using the fast Fourier transform (FFT) with a nominal frequency resolution of 0.017 Hz, based on a 60 s record. The resulting spectra are shown in Figs. 13(b)–13(d). Both the no-endplate and 2D-sized endplate cases show no clear dominant frequency, indicating the absence of coherent vortex structures. In contrast, the 3D-sized endplate configuration exhibits a strong spectral peak at $St = 0.18$, a value consistent with classical vortex shedding from a fixed circular cylinder. This observation suggests that the 3D-sized endplates help maintain organized vortex shedding even in the post-lock-in regime, where the structure is not actively oscillating, likely due to suppression of end effects.

Figure 14 presents the time-domain signals and corresponding frequency spectra of the lift coefficient and amplitude ratio for the configurations without endplates [Fig. 14(a)] and with 3D-sized endplates [Fig. 14(b)], which provide further evidence of the distinct aerodynamic behavior in the post-lock-in regime. In the no-endplate case, both the lift force and structural motion exhibit minimal fluctuation. The time-domain signal of C_L appears flat, and the corresponding frequency spectrum reveals no dominant frequency. Although the amplitude spectrum of A^* shows a very weak peak near the natural frequency, the amplitude ratio remains below 0.01, indicating that the cylinder is nearly stationary, experiencing only vibrations at the background noise level. In contrast, the 3D-sized endplate configuration displays a markedly different behavior. The lift coefficient shows noticeable unsteady fluctuations, and the frequency spectrum of C_L reveals a dominant peak at $St = 0.18$, consistent with coherent vortex shedding. Interestingly, the amplitude spectrum of A^* for this case shows two peaks: one corresponding to the natural frequency of the oscillator and the other near the vortex shedding frequency. This suggests that the cylinder is not perfectly stationary, but is undergoing small, irregular oscillations induced by the fluctuating aerodynamic forces, without establishing coherent harmonic motion.

It is also seen that there is a peak at 6.5 Hz in the amplitude response spectra for both the bare cylinder and the 3D-sized endplate configurations. Interestingly, no corresponding discrete peak is observed in the lift-force spectra, indicating that this vibration is not directly driven by strong, coherent aerodynamic forcing. Instead, the presence of the amplitude peak at 6.5 Hz in both cases likely results from weak or broadband flow disturbances. While these disturbances may not generate a strong spectral signature in the lift force, they are still capable of exciting a measurable structural response. Moreover, a comparison of the lift-force power spectral densities reveals elevated energy in the 6–9 Hz range for the 3D-endplate case relative to the bare cylinder, further supporting the presence of broadband aerodynamic excitation contributing to the observed weak structural response. Given the low damping and high sensitivity of the system, even small, random aerodynamic fluctuations arising from turbulent wake structures can induce small but detectable vibrations in the post-lock-in regime.

These findings demonstrate that while all configurations eventually settle into a mechanically stable state in the post-lock-in regime, the 3D-sized endplate configuration continues to exhibit intense unsteady aerodynamic behavior. In contrast, the wake responses for the bare cylinder and 2 D-sized endplate cases become negligible and largely unobservable.

D. Cylinder wake flow visualization analysis

To further elucidate the results in the pressure and force measurements, qualitative flow visualization was conducted to gain insight into the wake structures associated with different endplate configurations and flow regimes.

A complete set of flow visualization snapshots illustrating the pre-lock-in, lock-in, and post-lock-in regimes is provided in Fig. 15 for the bare cylinder and in Fig. 16 for the 3D-sized endplate configuration. Each figure includes the amplitude ratio vs reduced velocity plot, where specific flow visualization frames are annotated along the curve to indicate the corresponding operating points. These visualizations capture the evolution of the wake structure across all dynamic regimes, highlighting the changes in flow behavior relative to the system's vibration response. This combined view allows for direct correlation between oscillation amplitude, reduced velocity, and wake dynamics in both configurations.

Flow visualization during the pre-lock-in regime reveals no distinct vortex formation in any of the studied configurations. The wake appeared diffuse and lacked organized vortex shedding structures, indicating the absence of coherent unsteady flow dynamics. Notably, the addition of endplates did not introduce any significant change to the wake structure in this regime. The flow fields for the bare cylinder [Fig. 15(b)] and the 3D-sized endplate configuration [Fig. 16(b)] exhibit nearly identical wake behavior in the near field. While the no-endplate configuration did not show any clear patterns, the 3D-sized endplates produced some faint flow structures further downstream, approximately 2–3 cylinder diameters behind the body. However, no organized vortex shedding was observed near the cylinder surface, and these weak downstream features did not correlate with any significant lift force fluctuation. This qualitative observation is consistent with the force measurements, which showed no dominant frequencies or oscillatory forcing during the pre-lock-in regime (Fig. 9). These results confirm that at low velocities, structural flexibility suppresses vortex formation, and the endplates have negligible influence on near-wake dynamics.

Flow visualization during the lock-in regime revealed the onset of organized vortex shedding, coinciding with the start of structural

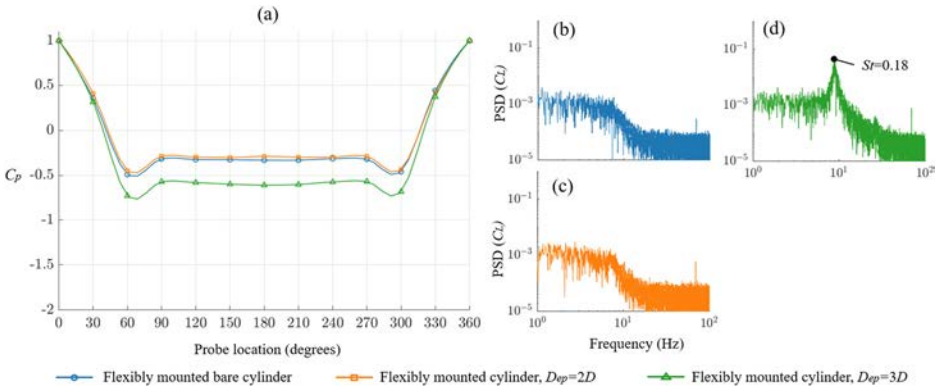

FIG. 13. Pressure coefficient distributions and lift force spectra for the flexibly mounted cylinder in the post-lock-in regime (3D endplates experimental set: m^*=146, ζ = 0.3%): (a) Pressure coefficient C_P; (b) C_L frequency spectrum of the bare cylinder; (c) C_L frequency spectrum of the cylinder with 2D endplates; and (d) C_L frequency spectrum of the cylinder with 3D endplates.

vibration. Remarkably, for all configurations, the initiation of lock-in occurred at a Strouhal number of approximately $St = 0.18$, indicating that the fundamental shedding frequency is preserved regardless of the presence or absence of endplates. Near the beginning of the initial branch (low-amplitude regime), the wake structure appeared nearly identical for the bare cylinder and the 3D-sized endplate configuration. Figures 15(c) and 16(c) show representative flow fields from both configurations at $U^* = 5.8$, confirming the visual similarity in vortex shedding structure and near-wake behavior at the early stage of lock-in. Both cases exhibited well-organized, alternating vortex shedding (2S mode) that was symmetrical and periodic in nature. This similarity in wake behavior was maintained up to an amplitude ratio of approximately $A^* \approx 0.3$. Beyond this threshold, differences in wake dynamics began to emerge as the system moved to the higher air velocities.

As the reduced velocity increases, the 3D-sized endplate configuration transitions to the lower branch of the VIV response at approximately $U^* = 6.3$, marked by a slight decrease in vibration amplitude following the peak. In contrast, the no-endplate configuration remains in the initial branch, where a continued increase in air velocity leads to higher amplitude vibrations. The difference in wake behavior between these two cases becomes especially pronounced at $U^* = 6.7$ [Figs. 15(d) and 16(d)]. At this velocity, both configurations operate at the same Reynolds number and exhibit similar oscillation frequencies, yet their wake structures diverge significantly—a clear illustration of the impact of endplates.

For the bare cylinder at $U^* = 6.7$ [Fig. 15(d)], the wake transitions from a classical 2S vortex shedding pattern to a 2P structure, where two pairs of vortices are formed per oscillation cycle. The vortex formation occurs very close to the cylinder surface, indicating strong flow-body coupling and large lift force fluctuation. In contrast, the 3 D-sized endplate configuration at the same velocity [Fig. 16(d)] also exhibits a 2P wake pattern, but with vortex formation shifted significantly farther downstream.

These visual observations are consistent with the lift force measurements at $U^* = 6.7$: the bare cylinder exhibits a high RMS lift coefficient of approximately 0.8, while the 3D-sized endplate configuration shows a significantly lower RMS value around 0.3. Despite similar upcoming flow and system conditions, the large disparity in lift fluctuation confirms that the presence of the endplates alters the fluid-structure interaction, shortening the duration of strong coupling between the flow and the structure in the initial branch.

As the reduced velocity continues to increase, the amplitude ratio curves for all configurations begin to merge in the lower branch around $U^* = 8.0 - 8.3$. At this point, the differences in vibration amplitude across configurations diminish, and the flow behavior becomes increasingly similar. Flow visualization at $U^* = 8.3$, corresponding to an amplitude ratio of approximately 0.15, reveals that the wake structures of the bare cylinder and the 3D-sized endplate configuration become nearly indistinguishable. As shown in Figs. 15(e) and 16(e), both configurations display a 2P vortex shedding pattern, with

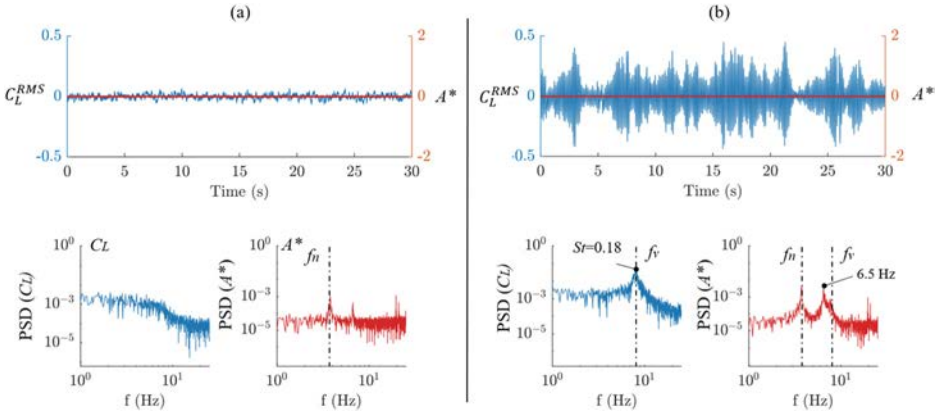

FIG. 14. Lift force and the response of the system (3D-sized endplates experimental set: m^*=146, f_n=3.74 Hz, ζ = 0.3%) in the post-lock-in region: (a) no-endplate with added mass and (b) with endplates of D_{ep}=3D.

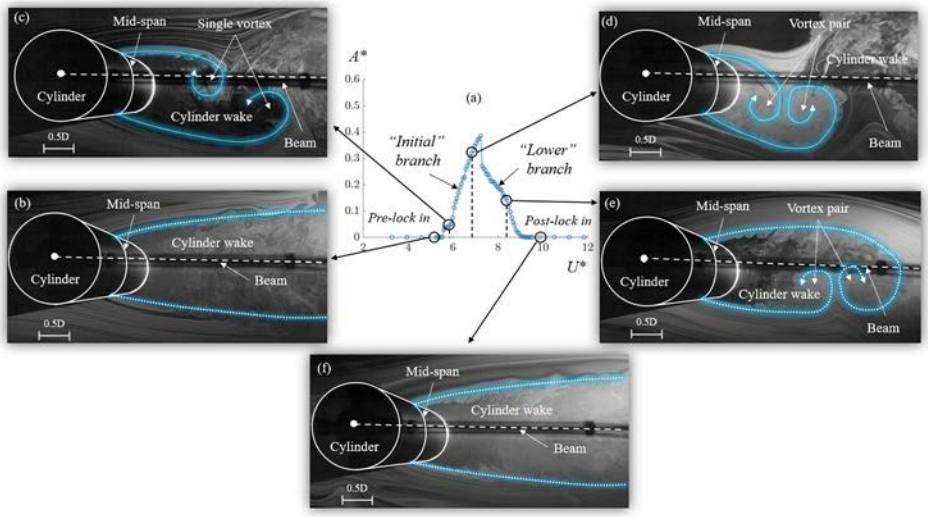

FIG. 15. Wake structure visualization of the no endplates configuration ($m*=146$, $\zeta = 0.3\%$): (a) Amplitude ratio vs reduced velocity plot; (b) pre-lock-in at $U^*=5$; (c) initial branch at $U^*=5.8$; (d) initial branch at $U^*=6.7$; (e) lower branch at $U^*=8.3$; and (f) post-lock-in at $U^*=10$.

vortex formation occurring further downstream as the flow velocity increases. This indicates a progressive elongation of the wake and a shift toward weaker flow-body coupling.

The observed similarity in wake behavior coincides with the merging of the amplitude response curves, suggesting that the influence of endplates becomes negligible in this regime. This is further supported by the force measurements shown in Fig. 10, where both the drag and lift coefficients also converge at approximately the same reduced velocity. Together, these observations confirm that beyond $U^* \approx 8.3$ of the lock-in the system enters a regime where endplate effects are no longer significant.

Flow visualization in the post-lock-in regime ($U^* > 9.2$) revealed a significant difference in wake behavior between the configurations with and without endplates. For the bare cylinder, no coherent vortex shedding patterns were observed. In contrast, the 3D-sized endplate configuration exhibited a well-defined Karman vortex street, characterized by alternating vortices shed downstream in a classic, symmetric pattern. This observation aligns closely with the lift force spectra presented in Fig. 14, in which the no-endplate case showed no significant fluctuation in C_L, while the 3D-sized endplate case displayed a strong spectral peak at $St = 0.18$.

V. CONCLUSIONS

This study presents a comprehensive experimental investigation into the three-dimensional effects of finite-length circular cylinder oscillators and examines the influence of endplates on their aerodynamic behavior and energy harvesting potential during vortex-induced vibration (VIV). Two configurations were examined: a rigidly mounted stationary cylinder, used as a reference case, and a flexibly mounted cylinder allowed to oscillate transversely under flow-induced excitation. For the stationary cylinder, five configurations were tested: a bare cylinder and cylinders with circular endplates of four different sizes. In the VIV experiments, three setups were evaluated: a bare cylinder and cylinders equipped with double-diameter and triple-diameter circular

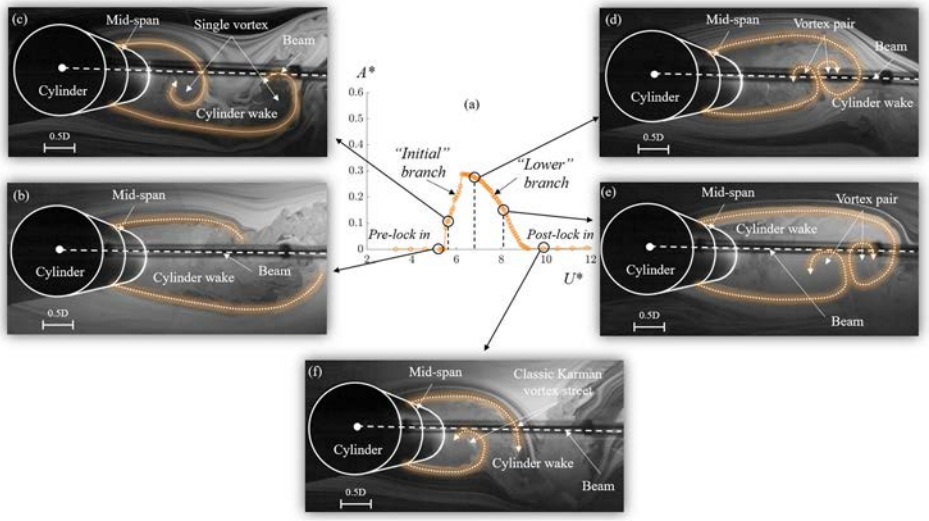

FIG. 16. Wake structure visualization of the 3D endplates configuration ($m*=146$, $\zeta = 0.3\%$): (a) Amplitude ratio vs reduced velocity plot; (b) pre-lock-in at $U^*=5$; (c) initial branch at $U^*=5.8$; (d) lower branch at $U^*=6.7$; (e) lower branch at $U^*=8.3$; and (f) post-lock-in at $U^*=10$.

endplates. The experiments explored the system behavior across the pre-lock-in, lock-in, and post-lock-in regimes using synchronized measurements of pressure distribution, structural response, force coefficients, and flow visualization.

The stationary cylinder results provided two key insights. First, they established a practical cutoff for endplate effectiveness: circular endplates with a diameter of approximately triple of the cylinder diameter are sufficient to suppress spanwise flow and reproduce aerodynamic behavior similar to that of an infinite-length cylinder. Larger sizes of the endplates offer no added benefit. Second, the addition of endplates significantly increases the fluctuation amplitude of lift coefficient, i.e., from $C_L^{RMS} \approx 0.05$ for the bare cylinder to $C_L^{RMS} \approx 0.19$ with endplates of sizes 3D and larger, highlighting their potential to enhance unsteady aerodynamic loading.

For the flexibly mounted cylinder, the system's response varied considerably. In the pre-lock-in regime, all configurations, regardless of the addition of endplates, exhibited minimal vortex formation and negligible lift fluctuations. This indicates that endplates have no significant aerodynamic effect prior to the onset of lock-in. In the lock-in regime, the bandwidth of vibration, as well as the onset and termination of synchronized oscillations, remained unaffected by the presence of endplates across all studied cases, including both the 2D- and 3D-sized endplate experimental sets. However, within the lock-in regime, the oscillation amplitude and aerodynamic response of the cylinder were highly dependent on the endplate size. This indicates that while endplates do not alter the window of the airflow velocity over which vibrations occur, they significantly influence the dynamics of the coupled fluid–structure interaction.

The 3D-sized endplate experimental set (m^*=146), in which mass differences between configurations were compensated, isolated the aerodynamic influence of the endplates on the system's dynamic response. In terms of oscillation amplitude response, the influence of endplates became evident in the initial branch starting from $U^* \geq 6.3$ (where $A^* \geq 0.3$) and persisted through the peak vibration into the lower branch past $U^* \leq 8.3$ (where $A^* \geq 0.15$). In terms of lift force response, both the 2D- and 3D-sized endplate cases showed a sudden, steeper rise in lift coefficient at the onset of the initial branch and higher peak values. However, after $U^* \geq 7.2$, in the lower branch, the lift coefficients for all configurations converged and remained nearly identical. The 3D-sized endplate configuration produced the most pronounced effect, shortening the initial branch, reducing the peak amplitude, and triggering an earlier transition into the lower branch, despite generating the most intense lift fluctuations among all configurations. In contrast, the 2D-sized endplates slightly increased the peak amplitude relative to the bare cylinder. These results demonstrate that the observed changes in oscillator behavior were predominantly driven by aerodynamic modifications due to the endplates, rather than by variations in structural inertia.

A comparison between the bare cylinder and configurations with 2D-sized endplates highlights the combined effects of endplate size and added mass. The bare cylinder without added mass (m^*=105) achieved a peak amplitude of A^*=0.47, while the same cylinder equipped with 2D-sized endplates (m^*=121) reached peak amplitudes of A^*=0.48, suggesting that although increased mass generally suppresses vibration amplitude, the aerodynamic benefit provided by the endplates can offset this effect, leading to a net gain in energy harvesting potential.

In the post-lock-in regime, the aerodynamic behavior diverged sharply between configurations. The lift force spectrum analysis (i.e., obtained based on the surface pressure measurements at the mid-span of the cylinder) for the bare cylinder and the 2D-sized endplate cases shows similar results with no dominant peak, indicating no coherent vortex shedding and a minimal flow-structure coupling state at the mid-span of the cylinder. In contrast, the 3D-sized endplates maintained organized vortex shedding, evidenced by the spectral peak at $St = 0.18$, even in the absence of significant transverse motion, highlighting their strong role in confining the flow and stabilizing vortex formation in the wake. These findings demonstrate that even when structural motion is suppressed due to high-frequency aerodynamic forcing ($f_v \gg f_n$), the use of endplates with sizes of three times the diameter or larger can effectively mitigate end effects and maintain unsteady flow conditions.

In summary, while endplates do not alter the onset or termination of the lock-in regime, they exert a critical influence on the system's dynamic response within resonance, fundamentally shaping the amplitude and nature of the coupled fluid-structure interaction. These findings underscore the significant impact of endplate size on VIV behavior and reveal promising design pathways for next-generation VIV-based energy harvesting systems. Beyond advancing the understanding of bluff body aerodynamics, this study opens new avenues for optimizing performance through deliberate geometric modifications of the oscillators.

ACKNOWLEDGMENTS

The research work was supported by the National Science Foundation (NSF) Award No. #2131600 and the Professional Staff Congress-City University of New York (PSC-CUNY) Enhanced Award.

AUTHOR DECLARATIONS

Conflict of Interest

The authors have no conflicts to disclose.

Author Contributions

Andrei Fershalov: Conceptualization (equal); Data curation (lead); Formal analysis (lead); Investigation (lead); Methodology (lead); Software (equal); Validation (lead); Visualization (lead); Writing – original draft (lead). **Niell Elvin:** Conceptualization (lead); Formal analysis (equal); Funding acquisition (lead); Investigation (equal); Methodology (equal); Project administration (lead); Resources (equal); Software (equal); Supervision (lead); Validation (equal); Visualization (equal); Writing – review & editing (equal). **Daniel Struk:** Data curation (equal); Investigation (equal); Methodology (equal); Software (equal); Visualization (equal). **Denise Morocho Romero:** Data curation (equal); Investigation (equal); Methodology (equal); Visualization (equal). **Pieter Orlandini:** Data curation (equal); Investigation (equal); Methodology (equal); Visualization (equal). **Yang Liu:** Conceptualization (equal); Formal analysis (equal); Funding acquisition (equal); Investigation (equal); Methodology (equal); Project administration (equal); Software (equal); Supervision (equal); Visualization (equal); Writing – review & editing (equal).

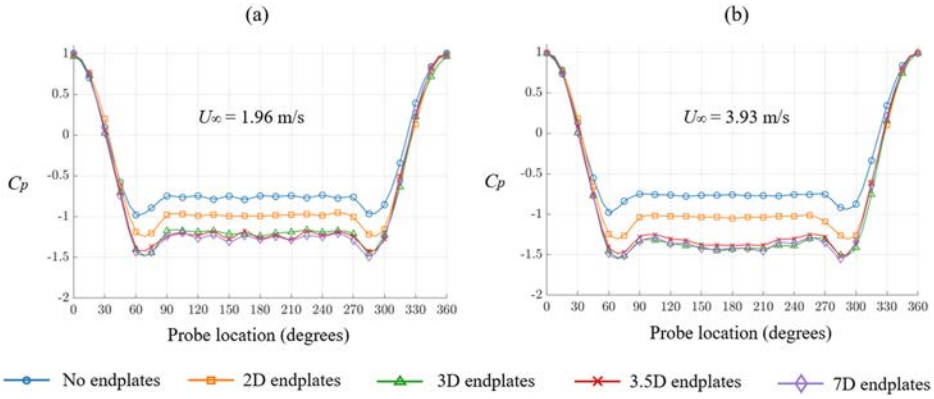

FIG. 17. Pressure coefficient distributions around the stationary cylinder (0° at the front stagnation point) for all endplate configurations at two air velocities: (a) 1.96 m/s and (b) 3.93 m/s.

TABLE I. Aerodynamic parameters for the stationary cylinder with different endplates.

Aerodynamic parameter	No endplates	2D-sized endplates	3D-sized endplates	3.5D-sized endplates	7D-sized endplates
Mean drag coefficient, C_D^{mean}	0.807	0.959	1.14	1.15	1.17
RMS of the lift coefficient, C_L^{RMS}	0.048	0.077	0.182	0.189	0.197
Strouhal number, St	0.183	0.202	0.212	0.212	0.215

DATA AVAILABILITY

The data that support the findings of this study are available from the corresponding author upon reasonable request.

APPENDIX: EFFECT OF ENDPLATES ON FLOW AROUND A STATIONARY CYLINDER

Figure 17 shows the pressure distributions around the cylinder for all five configurations, including bare cylinder and cylinder with endplates of four different sizes (2D, 3D, 3.5, and 7D), at 1.96 and 3.93 m/s. The measured C_p distributions remained consistent across the tested air velocities, indicating stable aerodynamic behavior. The results show that endplates have little effect on the upwind C_p (0°–45° and 315°–360°) but markedly deepen the downwind suction (45°–315°): the cylinder with 2D-sized endplates exhibited higher negative C_p values than the bare cylinder, while the cylinder with 3D-sized endplates showed an even further increase in the C_p magnitude. Once the endplate size exceeds 3D (i.e., 3.5D and 7D), the C_p profiles become essentially identical, indicating that further increases of the endplate size beyond 3D have a minimal effect, consistent with previous studies.[2]

In addition to the pressure coefficient distributions, the aerodynamic performance of the stationary cylinder was further evaluated using the drag and lift coefficients, as well as the Strouhal number. The drag coefficient C_D was calculated using the time-averaged drag force, representing the steady component of the flow-induced loading. The root mean square (RMS) of the lift coefficient C_L^{RMS} was used to assess the unsteady nature of the vortex shedding and its influence on transverse loading.

The Strouhal number St, characterizing the frequency of vortex shedding, was computed based on spectral analysis of the lift force signal, providing insight into the wake dynamics and their dependence on flow velocity and endplate configuration.

The experimental results for all configurations—including the drag and lift coefficients and Strouhal numbers—are summarized in Table I, which compares the aerodynamic effects introduced by the different endplate sizes under stationary conditions.

It is revealed that the addition of endplates significantly increases both drag and lift on the stationary cylinder. Compared to the no-endplate configuration, the time-averaged (mean) drag coefficient C_D^{mean} increases by more than 40% for the configures with 3D-sized endplates and larger, reflecting enhanced pressure drag due to the spanwise-flow suppression and wake modification. Similarly, introducing 2D-sized endplates boosts C_L^{RMS} by approximately 50%, while the endplates with sizes of 3D or greater elevate C_L^{RMS} to over 0.18—a more than threefold increase—indicating intensified vortex shedding and higher induced unsteady transverse loading. Finally, the Strouhal number increases modestly from 0.183 (for the no-endplate configuration) to 0.202–0.215 (for the cases with endplates), suggesting a slight upward shift in vortex shedding frequency.

REFERENCES

[1]D. A. Potts, J. R. Binns, A. E. Potts, and H. Marcollo, "The effect of aspect ratio on the drag of bare cylinders," in Proceedings of the ASME 2019 38th International Conference on Ocean, Offshore and Arctic Engineering (OMAE'19), Glasgow, Scotland, 2019.
[2]C. Farell and S. K. Fedeniuk, "Effect of end plates on the flow around rough cylinders," J. Wind Eng. Ind. Aerodyn. **28**, 219–230 (1988).
[3]C. Norberg, "An experimental investigation of the flow around a circular cylinder: Influence of aspect ratio," J. Fluid Mech. **258**, 287–316 (1994).
[4]C. Norberg, "Fluctuating lift on a circular cylinder: Review and new measurements," J. Fluids Struct. **17**(1), 57–96 (2003).
[5]P. W. Bearman, "Vortex shedding from oscillating bluff bodies," Annu. Rev. Fluid Mech. **16**, 195–222 (1984).
[6]T. Sarpkaya, "A critical review of the intrinsic nature of vortex-induced vibrations," J. Fluids Struct. **19**(4), 389–447 (2004).

[7]C. H. K. Williamson and R. Govardhan, "Vortex-induced vibrations," Annu. Rev. Fluid Mech. **36**, 413–455 (2004).
[8]A. Khalak and C. H. K. Williamson, "Investigation of the relative effects of mass and damping in vortex-induced vibration of a circular cylinder," J. Wind Eng. Ind. Aerodyn. **69–71**, 341–350 (1997).
[9]A. Khalak and C. H. K. Williamson, "Motions, forces and mode transitions in vortex induced vibrations at low mass-damping," J. Fluids Struct. **13**, 813–851 (1999).
[10]C. Feng, "The measurement of vortex induced effects in flow past stationary and oscillating circular and d-section cylinders," Ph.D. dissertation (University of British Columbia, Vancouver, Canada, 1968).
[11]P. Anagnostopoulos and P. W. Bearman, "Response characteristics of a vortex-excited cylinder at low Reynolds numbers," J. Fluids Struct. **6**(1), 39–50 (1992).
[12]R. Govardhan and C. H. K. Williamson, "Modes of vortex formation and frequency response for a freely-vibrating cylinder," J. Fluid Mech. **420**, 85–130 (2000).
[13]T. Shepard, D. Law, J. Dahl, R. Reichstadt, and A. S. Selvamani, "Impact of aspect ratio on drag and flow structure for cylinders with two free ends," J. Fluids Eng. **145**, 091301 (2023).
[14]T. Kitagawa, Y. Fujino, and K. Kimura, "Effects of free-end condition on end-cell-induced vibration," J. Fluids Struct. **13**(4), 499–518 (1999).
[15]L. Zhang, A. Abdelkefi, H. Dai, R. Naseer, and L. Wang, "Design and experimental analysis of broadband energy harvesting from vortex-induced vibrations," J. Sound Vib. **408**, 210–219 (2017).
[16]H. D. Akaydin, N. G. Elvin, and Y. Andreopoulos, "The performance of a self-excited fluidic energy harvester," Smart Mater. Struct. **21**(2), 025007 (2012).
[17]V. Azadeh-Ranjbar, N. G. Elvin, and Y. Andreopoulos, "Vortex-induced vibration of finite-length circular cylinders with spanwise free-ends: Broadening the lock-in envelope," Phys. Fluids **30**, 105104 (2018).
[18]Z. Lai, S. Wang, L. Zhu, G. Zhang, J. Wang, K. Yang, and D. Yurchenko, "A hybrid piezo-dielectric wind energy harvester for high-performance vortex-induced vibration energy harvesting," Mech. Syst. Signal Process. **150**, 107212 (2021).
[19]A. Erturk and D. J. Inman, *Piezoelectric Energy Harvesting* (John Wiley & Sons, New York, USA, 2011).
[20]H. D. Akaydin, N. G. Elvin, and Y. Andreopoulos, "Wake of a cylinder: A paradigm for energy harvesting with piezoelectric materials," Exp. Fluids **49**(2), 291–304 (2010).
[21]H. D. Akaydin, N. Elvin, and Y. Andreopoulos, "Energy harvesting from highly unsteady fluid flows using piezoelectric materials," J. Intell. Mater. Syst. Struct. **21**(13), 1263–1278 (2010).
[22]O. Goushcha, H. D. Akaydin, N. Elvin, and Y. Andreopoulos, "Energy harvesting prospects in turbulent boundary layers," J. Fluids Struct. **54**, 823–847 (2015).
[23]A. Fershalov, N. Elvin, P. Orlandini, I. Avros, and Y. Liu, "Harvesting sustainable energy through vortex-induced vibrations of finite length cylinder," Phys. Fluids **37**(4), 044108 (2025).
[24]F. Pan, Z. Xu, P. Pan, and L. Jin, "Piezoelectric energy harvesting from vortex-induced vibration using a modified circular cylinder," in *2017 20th International Conference on Electrical Machines and Systems (ICEMS)* (IEEE, 2017).
[25]M. Verma and A. De, "Dynamics of vortex-induced vibrations of a slit-offset circular cylinder for energy harvesting at low Reynolds number," Phys. Fluids **34**, 083607 (2022).
[26]U. Javed and A. Abdelkefi, "Characteristics and comparative analysis of piezoelectric-electromagnetic energy harvesters from vortex-induced oscillations," Nonlinear Dyn. **95**, 3309–1950 (2019).
[27]I. Patrick, S. Adhikari, and M. I. Hussein, "Metaharvesting: Emergent energy harvesting by piezoelectric metamaterials," Proc. R. Soc. London, Ser. A **480**, 20240033 (2024).
[28]D. Cao, X. Guo, J. Wang, and S. K. Lai, "Recent advancement of flow-induced piezoelectric vibration energy harvesting techniques: Principles, structures, and nonlinear designs," Appl. Math. Mech. Engl. Ed. **43**, 959–1472 (2022).
[29]S. Bakhtiar, F. Khan, A. Z. Hajjaj, and H. Fu, "Fluid flow-based vibration energy harvesters: A critical review of state-of-the-art technologies," Appl. Sci. **14**, 11452 (2024).
[30]P. Han, Q. Huang, G. Pan, D. Qin, W. Wang, R. T. Goncalves, and J. Zhao, "Optimal energy harvesting efficiency from vortex-induced vibration of a circular cylinder," Ocean Eng. **282**, 114869 (2023).
[31]M. Zhang and J. Wang, "Experimental study on piezoelectric energy harvesting from vortex-induced vibrations and wake-induced vibrations," J. Sens. **2016**(2), 1–7.
[32]M. Zhang, C. Zhang, A. Abdelkefi, H. Yu, O. Gaidai, X. Qin, H. Zhu, and J. Wang, "Piezoelectric energy harvesting from vortex-induced vibration of a circular cylinder: Effect of Reynolds number," Ocean Eng. **235**, 109378 (2021).
[33]G. Hu, K. C. S. Kwok, K. T. Tse, and J. Song, "Aerodynamic modification to a circular cylinder to enhance the piezoelectric wind energy harvesting," Appl. Phys. Lett. **109**(19), 193902 (2016).
[34]C. Xia, L. Tang, P. Yin, and K. C. Aw, "Multi-directional and multi-modal vortex-induced vibrations for wind energy harvesting," Appl. Phys. Lett. **125**(20), 203901 (2024).
[35]M. L. Facchinetti, E. de Langrea, and F. Biolley, "Coupling of structure and wake oscillators in vortex-induced vibrations," J. Fluids Struct. **19**(2), 123–140 (2004).
[36]K. Xu, Y. Ge, and D. Zhang, "Wake oscillator model for assessment of vortex-induced vibration of flexible structures under wind action," J. Wind Eng. Ind. Aerodyn. **136**, 192–200 (2015).
[37]Y. Qu and A. V. Metrikine, "A wake oscillator model with nonlinear coupling for the vortex-induced vibration of a rigid cylinder constrained to vibrate in the cross-flow direction," J. Sound Vib. **469**, 115161 (2020).
[38]J. H. Lienhard, "Synopsis of lift, drag, and vortex frequency data for rigid circular cylinders," Technical Report No. 300 (Washington State University, College of Engineering Research Division, 1966).
[39]S. S. Rao, *Mechanical Vibrations*, 6th ed. (Pearson, Boston, MA, USA, 2017).
[40]Y. Liao and H. A. Sodano, "Model of a single mode energy harvester and properties for optimal power generation," Smart Mater. Struct. **17**(6), 065026 (2008).
[41]Y. Andreopoulos and A. Honkan, "An experimental study of the dissipative and vortical motion in turbulent boundary layers," J. Fluid Mech. **439**, 131–163 (2001).
[42]C.-K. Choi and D.-K. Kwon, "Wind tunnel blockage effects on aerodynamic behavior of bluff body," Wind Struct. **1**(4), 351–364 (1998).
[43]R. N. Govardhan and C. H. K. Williamson, "Defining the 'modified griffin plot' in vortex-induced vibration: Revealing the effect of Reynolds number using controlled damping," J. Fluid Mech. **561**, 147–180 (2006).
[44]J. K. Vandiver, "Damping parameters for flow-induced vibration," J. Fluids Struct. **35**, 105–119 (2012).